

# Tuning and predicting the onset of desiccation cracks in air-dried aqueous clay suspensions

Vaibhav Raj Singh Parmar<sup>a</sup>, Ranjini Bandyopadhyay<sup>a,1</sup>

<sup>a</sup>Soft Condensed Matter Group, Raman Research Institute, C. V. Raman Avenue, Sadashivanagar, Bangalore, 560 080, India

---

## Abstract

**Hypothesis:** Stacks of clay platelets in aqueous suspension swell and break up gradually, with the exfoliated clay particles eventually self-assembling to form transient, fragile, gel-like networks. As a consequence of this physical aging phenomenon, clay suspensions transform spontaneously from viscoelastic liquids to viscoelastic solid-like phases. When subjected to desiccation, these colloidal systems accumulate drying-induced stresses and are prone to cracking. For a fixed evaporation rate and sample-boundary adhesion, it should be possible to control the formation of cracks by tuning the sample aging dynamics.

**Experiments:** Clay suspensions layers were dried in controlled environments. The location and time of crack onset were recorded in imaging experiments. The elasticity of each partially dried sample was extracted by performing microindentation experiments in an atomic force microscope.

**Findings:** Clay aging dynamics and desiccation crack onset were controlled by tuning clay and salt concentrations in the aqueous medium. Our experiments reveal that the crack onset time,  $t_c$ , varies with sample elasticity,  $E$ , according to  $t_c \propto 1/\sqrt{E}$ . We explain this correlation by proposing a simple scaling argument that incorporates the Griffith's fracture criterion in a poroelastic model. Fits to our model reveal the high ductility of aging clay suspensions. Besides allowing us to control the cracking process by tuning sample elasticity, our results are potentially useful in formulating crack-resistant coatings and paints.

**Keywords:** Desiccation cracks, Clay suspension, Microindentation, Poroelasticity, Fracture energy, Griffith theory of fracture

---

## 1. Introduction

Evaporating films, coatings and surface layers constituted by aqueous colloidal suspensions tend to shrink and crack [1, 2, 3, 4, 5, 6]. As water evaporates from colloidal samples, the air-water interface at the free evaporation surface develops a meniscus, resulting in enhanced internal pore pressure. Tensile stresses that build up in the sample due to desiccation-induced shrinkage are sensitively dependent on the adhesion of the sample with the frictional substrate [3, 7]. As the tensile stresses exceed the tensile strength of the material, the sudden release of stresses at the surface of the sample results in the formation of fractures/cracks. Once a crack is nucleated, its growth kinetics follow the Griffith's criterion [8], with the released strain energy exceeding the energy required to create new fracture surfaces [6]. Drying-induced cracks form successively, such that a previously formed crack determines the new stress field governing the formation of a new crack [7]. In such hierarchical crack patterns, a new crack meets an existing one at  $90^\circ$ . In contrast, for very thin drying layers [9] and samples undergoing repeated drying and wetting cycles [10], crack joint angles of  $120^\circ$  have been reported.

Crack formation is a complex phenomenon observed over a range of length scales and in various systems such as monolayers of microbeads [11], old paintings [12], craquelures in pottery glaze [1], industrial coatings [4], colloidal crys-

tals [13], crocodile head scales [14], columnar jointing in cooling lava [15] and dried lakes [16]. Though undesirable in many applications, understanding drying-induced cracks is useful in the investigation of ancient geophysical processes [15], identifying health problems by drying drops of blood [17], as a forensic tool for monitoring drying blood pools in crime scenes [18] and while detecting the authenticity of old paintings [12, 19]. Morphological changes in crack patterns also reveal memory formation in drying pastes [20]. The morphologies and growth kinetics of desiccation cracks in drying colloidal samples depend on the evaporation rate [21], initial volume fraction [22], rheology of the material [23, 24], shapes [25], sizes [26] and surface charges of the constituent colloidal particles [27], sample thickness [9, 28, 29], substrate-sample adherence [9, 30], substrate wettability, applied fields [26, 31], substrate elasticity [32] and shape of the confining boundary [33].

Desiccation cracks in soils are particularly interesting due to their geophysical relevance [6, 34, 35]. Clay, a major ingredient of natural soil, exhibits very interesting rheology when mixed in water, with the initially liquid-like clay suspension losing its ability to flow and evolving gradually into a viscoelastic solid *via* a physical aging mechanism [36, 37, 38, 39]. Physical aging is a common phenomenon that appears in various systems such as colloidal gels [37, 40, 41], molecular glasses [42] and amorphous polymers [43]. It has been established that aging a gel before drying increases gel network strength and reduces the risk of fracture formation [44, 45, 46, 47]. While cracking because of solvent loss has been studied in great detail, the effect

---

<sup>1</sup>Corresponding author email: ranjini@rri.res.in

of physical aging of the sample during desiccation has received less attention. Here, we show *via* experiments and theory that the risk of fracturing of an isotropic gel-like aging clay sample can be evaluated from its mechanical properties in the fully-developed state.

In this paper, we report experiments on desiccation-induced crack formation in thin aqueous layers of the synthetic clay Laponite<sup>®</sup>. In powder form, monodisperse disk-shaped Laponite clay nanoparticles of 25 nm diameter and 1 nm thickness are arranged in one-dimensional stacks or tactoids. When this powder is mixed with water, the soluble Na<sup>+</sup> ions that reside in the interlayer gallery spaces [36] migrate towards the bulk aqueous medium due to osmotic pressure gradients. To maintain overall charge neutrality, the faces of the clay particles acquire negative charges. Screened electrostatic double layer repulsions between the faces of like-charged clay particles within the tactoids cause tactoid swelling and exfoliation [40, 48], as illustrated in Supplementary Information Fig. S1(a). Diffuse electric double layers of Na<sup>+</sup> ions that form around the negatively charged clay particles faces evolve with time as tactoid exfoliation progresses gradually [49, 50]. If the medium pH < 11, the clay particle edges acquire slight positive charges due to the hydration of magnesia groups [51, 52]. Individual disk-shaped clay particles in aqueous suspensions therefore have negative faces and positive rims, and spontaneously self-assemble into overlapping coin and house of cards configurations, as shown in Supplementary Information Fig. S1(b,c). The gradual formation and restructuring of system-spanning fragile clay gel networks result in a continuous increase in suspension elasticity [40, 48, 52, 53].

As shown schematically in Figs. 1(a,b), the addition of common salt leads to a reduction in double-layer repulsion and a strong temporal increase in the mechanical properties of the clay suspension due to accelerated structural buildup. When tetrasodium pyrophosphate is introduced to the medium, the attachment of P<sub>2</sub>O<sub>7</sub><sup>4-</sup> groups to clay particle rims enhances interparticle repulsions, ruptures suspension microstructures and fluidises the sample [54, 55]. Moreover, the aging dynamics of clay suspensions can be accelerated by increasing clay concentration [49]. Systematic studies of the evolution of the mechanical response of aging clay suspensions [37, 38, 39] due to the incorporation of additives [49, 56, 57], application of electric fields [58, 59, 60] and by tuning the solvent temperature and pH [51, 57] are available in the literature.

Since clay is a major ingredient of soil, there have been several attempts to understand the formation of desiccation cracks in thin contracting clay layers. In one such study, it was reported that the cumulative crack area decreased monotonically with increase in the ratio of the minimum crack width and clay layer thickness [35]. Interestingly, a combined experimental and numerical study demonstrated that the addition of polymers to clay suspensions can substantially modify desiccation crack morphologies [61]. It was reported that crack onset could be accelerated by increasing the strength of a static electric field [62]. Enhanced cracking was also reported when alternating voltages of progressively larger amplitudes and frequencies were applied [63]. A transition from multi-mode to single-mode periodic

crack features was noted when the amplitude of the alternating voltage was increased. These results were modelled successfully using a spring chain model.

We performed direct visualisation experiments and digital image correlation analyses to monitor the time and location of crack onset in desiccating clay layers. We recorded the time,  $t_c$ , at which the sample first cracks, and noted that the first crack always appears near the vertical boundary of the sample cell. We demonstrate here that crack formation can be promoted or inhibited by respectively adding common salt or tetrasodium pyrophosphate to the aqueous suspension medium. We measured the elasticity,  $E$ , of each partially dried sample by performing microindentation experiments in an atomic force microscope and observed that crack onset time  $t_c \propto 1/\sqrt{E}$ . Furthermore, by controlling the rate of water evaporation,  $V_E$ , from the drying sample by tuning the chamber temperature, we noted that  $t_c \propto 1/V_E$ . We explain our results by incorporating the Griffith's criterion for crack formation in a poroelastic formalism. Besides describing our experimental data successfully, our model allows us to estimate a fracture energy of  $\approx 10^3$  J/m<sup>2</sup> for the drying clay suspension layers studied here. These samples are therefore highly ductile and deform significantly before crack onset. Our study establishes that the formation of desiccation cracks can be controlled by tuning the sample aging dynamics. Since clay is a widely used rheological modifier, our results are useful in the formulation of crack-resistant films, coatings [64] and paints.

## 2. Materials and methods

### 2.1. Sample preparation

Hygroscopic Laponite<sup>®</sup> XLG powder was procured from BYK Additives Inc. and baked at 120°C for 18 – 24 hours to remove moisture. Aqueous solutions were prepared by adding a specific amount of sodium chloride, NaCl (common salt, LABORT Fine Chem Pvt. Ltd), or tetrasodium pyrophosphate, TSPP (E. Merck (India) Ltd), to deionized and distilled water (Millipore Corp., resistivity 18.2 MΩ-cm). A predetermined amount of dried Laponite powder was slowly added to 50 ml Milli-Q water to prepare clay sample without additive, or to an aqueous solution prepared with an additive (NaCl or TSPP) under vigorous stirring conditions. Homogeneous suspensions with clay concentrations 2.0, 2.5, 3.0 and 3.5% w/v were prepared using this method. After 40 minutes of vigorous mixing of the transparent clay suspension, 200 μl of 2.09 mM/L Rhodamine B dye was added to enhance contrast during imaging. Finally, the dyed clay suspensions were stirred for an additional 5 minutes.

### 2.2. Monitoring the physical aging phenomenon in clay suspensions via rheological measurements

To understand the evolution of microstructures in aging clay suspensions, oscillatory rheological measurements at 0.1% strain were performed at 25°C in an Anton Paar MCR702 rheometer while using a double gap geometry (DG26.7). Figure 1(b) shows the distinct time-evolution behaviours of complex viscosity  $\eta^* = \sqrt{G'^2 + G''^2}/\omega$  for suspensions with and

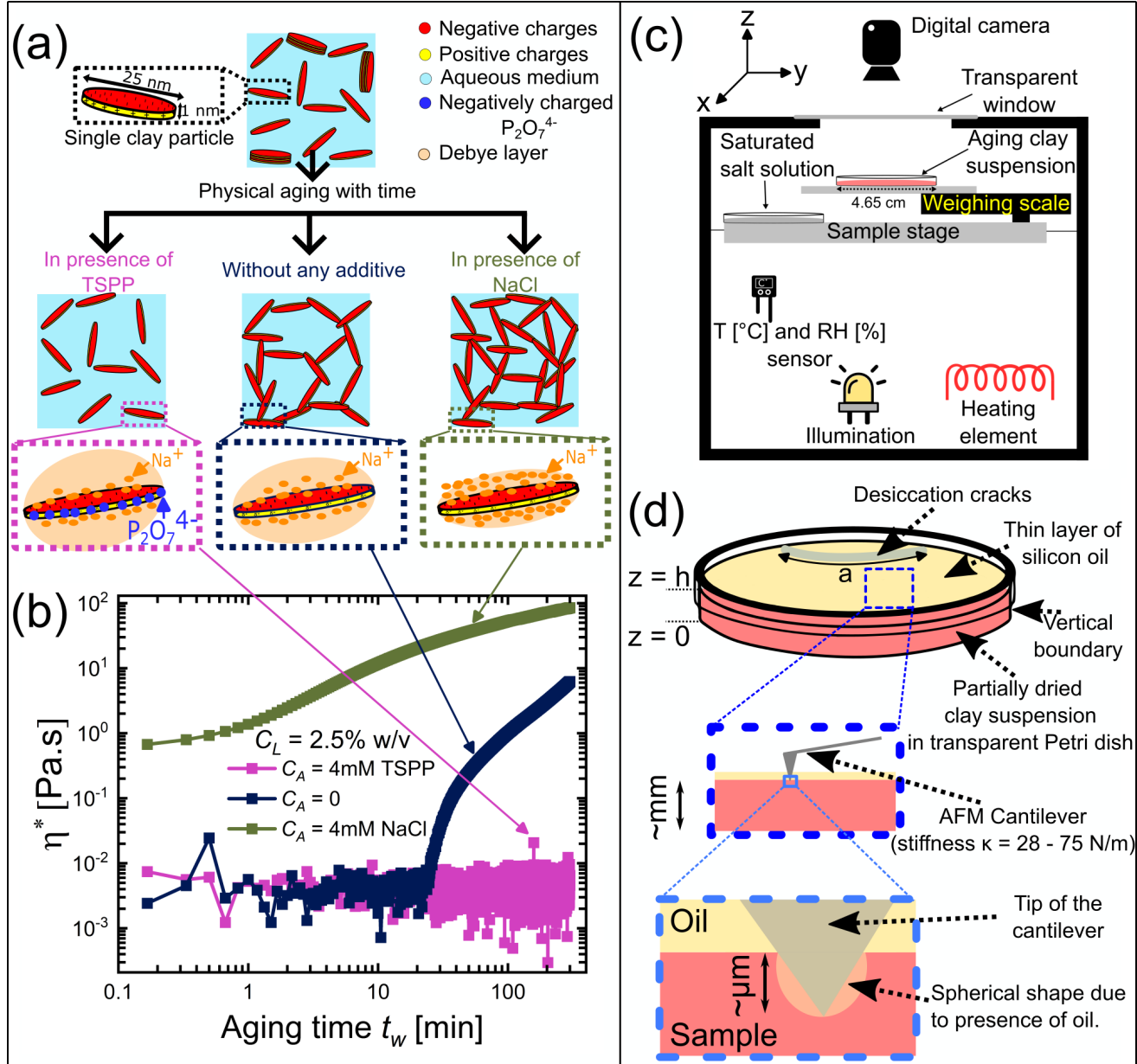


**Figure 1: Physical aging of aqueous Laponite clay suspensions, oscillatory time sweep rheology, experimental setup, and AFM microindentation measurements.** (a) Schematic illustration of the self-assembly of clay particles in suspensions with and without additives. (b) Temporal evolution of complex viscosity,  $\eta^* = \sqrt{G'^2 + G''^2} / \omega$ , of aqueous Laponite suspensions with no additive (navy blue), 4mM NaCl (olive green) and 4 mM TSPP (fucsia) at 25°C. Here,  $G'$  and  $G''$  are, respectively, the elastic and viscous moduli of the suspension and were measured in rheology experiments at a small strain  $\gamma = 0.1\%$  and angular frequency  $\omega = 6 \text{ rad/sec}$ . (c) Schematic diagrams of the experimental setup for imaging the onset and growth of desiccation cracks. (d) Schematic diagrams of a partially dried sample and a microindentation measurement performed to estimate sample elasticity. A thin layer of silicon oil was applied to the sample surface to reduce capillary attraction between the AFM cantilever and the sample.

without additives. In the presence of NaCl, the rapid evolution of  $\eta^*$ , plotted in Fig.1(b), indicates the enhanced formation of suspension microstructures [49, 57]. The presence of externally added  $Na^+$  and  $Cl^-$  ions shrinks the Debye layer surrounding each clay particle (Fig 1(a)), thereby reducing interparticle repulsion and promoting particle self-assembly in overlapping and house of cards configurations that eventually span the

entire system [52]. In contrast, the low and approximately constant  $\eta^*$  values in the presence of TSPP arise due to the absence of system-spanning microstructures in these repulsive suspensions.

### 2.3. The desiccation experiment

12 ml of the freshly prepared suspension was poured into a transparent polymethylpentene (TPX) Petri dish with an inner diameter of 4.65 cm. The initial clay layer thickness was kept constant at 7 mm in all the desiccation experiments reported here. The Petri dish was placed immediately in a temperature and humidity-controlled chamber, a schematic illustration of which is presented in Fig. 1(c). The temperature in the chamber was maintained at 35, 40, 45 and 50 °C in separate experimental runs using Arduino-based relay switching of a heating element. Humidity was maintained at  $27 \pm 4\%$  by placing a saturated salt solution of magnesium chloride in the chamber [65]. The variations of temperature and relative humidity inside the chamber during the experiment, shown in Supplementary Information Fig. S2, were seen to be minimal. The cracking of the drying suspension layer was recorded using a Nikon D5600 camera, with consecutive images taken at 3-minute intervals. Depending on the chamber temperature, the total drying duration of all the samples studied here varied between 22 and 46 hours.

#### 2.3.1. Imaging crack onset and propagation

A representative video of the temporal evolution of a desiccating sample with clay concentration of 3.0% w/v and NaCl concentration of 4mM is presented in Supplementary Video 1. The acquired images were converted to grayscale format and analysed using the MATLAB@2021 image processing toolbox. These images were binarized after setting a threshold. We recorded the time of crack onset,  $t_c$ , by determining the instant at which the first crack appeared. The procedure for determining  $t_c$  is schematically illustrated in Supplementary Information Fig. S3.

The Petri dish was placed on an Arduino-controlled weighing scale (Fig 1(c)) with a transparent acrylic measuring plate. The mass of the drying sample was monitored at intervals of 10 minutes. Supplementary Information Fig. S4 shows a monotonic decrease in the mass of the aqueous sample till the completion of evaporation. The evaporation rate,  $V_E$ , was determined from the change in sample mass due to loss of solvent, using  $V_E = \frac{dm/dt}{\pi\rho_w r^2}$  [66]. Here,  $dm/dt$  is the mass loss per unit time,  $\rho_w = 1 \text{ g/cm}^3$  is the density of water and  $\pi r^2$  is the area occupied by the evaporating clay surface in the Petri dish of radius  $r = 2.325 \text{ cm}$ . The temporal variation of the evaporation rate,  $V_E$ , is shown in Supplementary Information Fig. S4. The sample, prepared at room temperature, initially equilibrates to 50°C, after which we note distinct evaporation zones. After maintaining a constant rate for a few hours,  $V_E$  decreases rapidly to zero as the sample dries up. These distinct evaporation regimes were earlier also reported for drying nanopore gels [30] and wet granular media [67]. As in earlier observations [34, 68], we note that the first crack emerges during the constant evaporation rate regime in all our desiccating samples.

#### 2.3.2. Strain field analysis using digital image correlation

A random texture was created by sprinkling fine black pepper powder over the surface of the drying clay samples. The deformation of the texture due to desiccation-induced strains was

imaged and analysed using an open-source 2D digital image correlation (DIC) Matlab software ‘Ncorr’ [69, 70]. Ncorr determines one-to-one correspondences between a reference and subsequent images to estimate the deformation fields in the drying sample using linear combinations of translation, shear and stretch transformations. This protocol is used to evaluate the diagonal components of the two-dimensional strain tensor and estimate the extents of elongative and compressive stresses on the sample surface. Highly elastic Laponite suspensions of particle concentration 3.0% w/v and NaCl concentration 4 mM were studied to ensure only deformation and no flow during DIC analysis. Supplementary Video 2 shows the temporal evolution of drying clay suspensions for different sample-boundary adhesion conditions. Snapshots of these samples at various stages of drying are shown in Supplementary Information Fig. S5.

#### 2.4. Determining sample elasticity by microindentation using atomic force microscopy

The elasticity of partially dried clay samples was determined using a microindentation technique [71] in an atomic force microscope (Asylum Research, Oxford Instruments). The clay samples were allowed to dry for  $t = 14\text{h}$  or  $15\text{h}$  to ensure fully-developed gel structures when elasticity measurements were performed [49, 57]. Since clay samples contain water, microindentation can measure force with changing indentation depth only when capillary attraction between the cantilever (Tap190-G, stiffness = 28 - 75 N/m (Budget Sensors)) and sample is minimal. As illustrated in Fig. 1(d), a thin layer of silicon oil (Sigma-Aldrich) of viscosity  $\eta = 5 \text{ cSt}$  was applied on the surface of the partially dried sample to reduce capillary attraction between the cantilever and sample. The protocol adopted for measuring force-indentation depth curves is presented in section ST1 and Fig. S6 of the Supplementary Information. The force  $F(\delta)$  at an indentation depth  $\delta$  was estimated from raw AFM data. A representative force-indentation depth curve corresponding to a clay sample of particle concentration 2.5% w/v and NaCl concentration 4mM for  $\delta \geq 0$  is presented in Supplementary Information Fig. S6(e). Indentation experiments could not be performed for clay samples with added TSPP due to immeasurably low elasticity values.

Even though the tip of the cantilever used in these experiments is pyramid-shaped, the oil on the cantilever is expected to assume a spherical shape due to surface tension. This is illustrated in Fig. 1(d). The force-indentation depth curve was fitted with the Hertz contact model for a spherical tip,  $F(\delta) = \frac{4E\sqrt{R}\delta^{3/2}}{3(1-\nu^2)}$ , to extract sample elasticity,  $E$ , from the approaching cycle of the force-indentation depth curve. Here,  $\nu = 0.5$  is the Poisson’s ratio and  $R = 10 \text{ nm}$  is the cantilever-tip radius. Force-indentation depth data for a standard polymer sample (PDMS), acquired using microindentation and fitted to the Hertz model, yielded a reasonable elasticity value of 1.62 MPa, as shown in Supplementary Information Fig. S7.

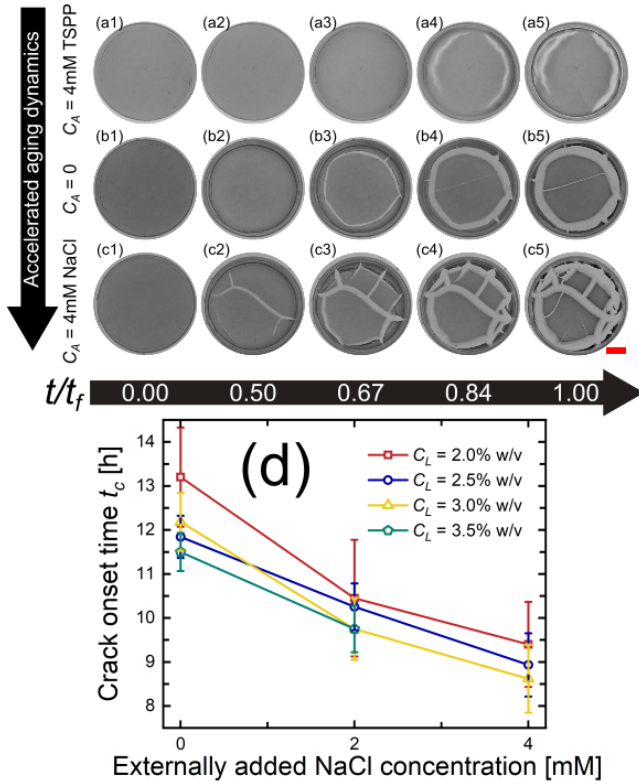


Figure 2: **Onset of desiccation cracks.** Time evolution of desiccation cracks in aging Laponite clay suspensions of particle concentration  $C_L = 2.5\%$  w/v as the solvent evaporates in the presence of (a1-a5) externally added TSPP of concentration 4 mM, (b1-b5) no additives and (c1-c5) externally added NaCl of concentration 4 mM. Here,  $t$  is the time elapsed since suspension loading and  $t_f$  is the total time duration for completion of the desiccation experiment. The scale bar at the bottom right of (c5) is 1 cm. (d) The crack onset time  $t_c$ , defined as the time elapsed when the first crack forms, decreases with increasing NaCl and clay concentrations. The error bars represent standard errors calculated from 3-4 experiments.

### 3. Results and discussions

#### 3.1. Accelerated aging in clay suspensions leads to earlier onset of cracks

In our first set of desiccation experiments, the evaporation rate of the sample was fixed by maintaining a constant temperature of  $50^\circ\text{C}$  and relative humidity of 27% in the experimental chamber. The aging dynamics, and therefore the rate of microstructural buildup of the sample, was tuned by controlling clay and additive concentrations. Figures 2(a-c) display the temporal evolution of desiccation cracks in drying clay suspensions, prepared at a concentration 2.5% w/v, both with and without additives. The horizontal axis shows the normalized elapsed time  $t/t_f$ , where  $t$  is the elapsed time and  $t_f$  is the total time required for completion of the desiccation process. Addition of TSPP (Figs. 2(a1-a5)) resulted in the lateral shrinkage of the drying sample, which detached from the Petri dish wall without the formation of desiccation cracks. For the clay suspension without additive (Figs. 2(b1-b5)), cracks formed before the occurrence of lateral shrinkage. In the presence of NaCl

(Figs. 2(c1-c5)), the first crack appeared even earlier and cracking increased substantially.

Clearly, solvent loss due to evaporation and the accelerated buildup of suspension microstructures in the aging sample both contribute to consolidating the drying clay sample and accelerating the onset of desiccation cracks. Crack onset time vs. added NaCl concentration is plotted in Fig. 2(d) for different clay concentrations. We observe that cracks form earlier with increase in salt and clay concentrations. Although the first crack always forms in the constant evaporation rate regime, there is a large standard deviation in the crack onset times, presumably due to local strain field heterogeneities in the drying samples. The final crack patterns, imaged after completion of the desiccation process, are shown in Supplementary Information Fig. S8(a). The surface crack ratio, which is a measure of the extent of crack formation, is estimated by dividing the total crack area by the total surface area of the drying sample. As expected, the surface crack ratio, plotted in Fig. S8(b), is higher for samples with larger NaCl content.

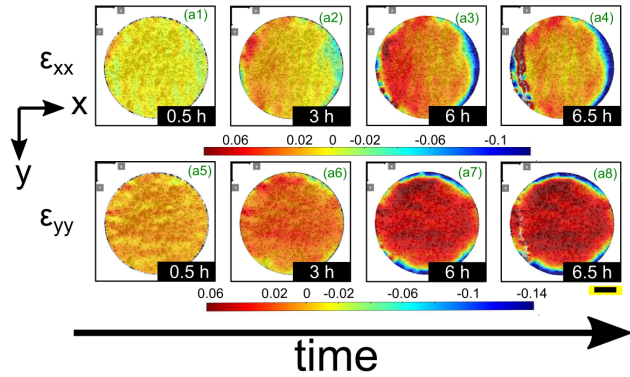


Figure 3: **Mapping strain fields during desiccation.** Temporal evolution of strain fields along the x and y directions,  $\epsilon_{xx}$  and  $\epsilon_{yy}$ , are displayed vs. elapsed time for a drying Laponite clay suspension of concentration 3.0% w/v with 4 mM externally added NaCl. The colour bars at the bottom of each row show the magnitudes of  $\epsilon_{xx}$  and  $\epsilon_{yy}$ , with positive and negative strain values indicating elongative and compressive strains respectively. The time stamps at the bottom right of each sub-figure indicate the elapsed time. The scale bar is 1 cm.

#### 3.2. Strain field maps reveal that the first crack nucleates at the vertical wall of the Petri dish

Figure 3 displays the strain fields on the surface of a drying clay sample of concentration 3.0% w/v with 4 mM added NaCl, analysed from the captured images using digital image correlation. Figures 3(a1-a4) and 3(a5-a8) show the evolutions of the diagonal components,  $\epsilon_{xx}$  and  $\epsilon_{yy}$ , of the strain tensor till the formation of the first crack. Estimates of elongative (+ve values) and compressive (-ve values) strains along the x and y directions, with the first image frame as reference, are represented by colour bars at the bottom of each row of figures. It is seen from Figs. 3(a1-a8) that while strong compressive strains develop near the vertical boundary as drying progresses, elongative strains are comparatively more uniformly distributed across the sample surface. In all the samples studied, the first crack

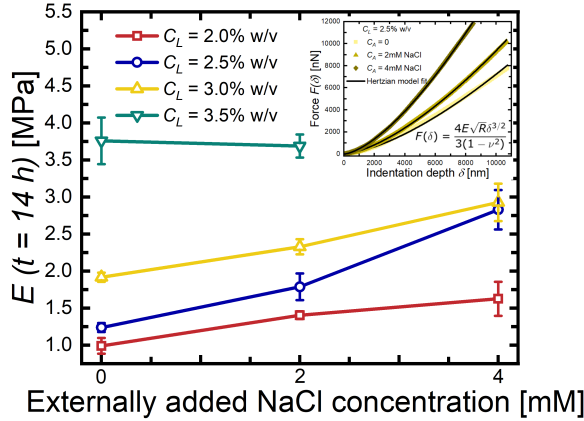


Figure 4: **Elasticity values.** The inset displays representative force-indentation depth curves for partially dried Laponite clay suspensions of concentration 2.5 % w/v with different NaCl contents at  $t = 14$  h. The sample elasticity values,  $E$ , in the main figure are extracted from the fits of the force-indentation depth data, shown by black lines in the inset, to the Hertz model. Standard errors in  $E$  are calculated from 3-8 measurements.

forms near the vertical wall of the Petri dish, where the buildup of adhesion-induced strains is strongest due to constrained lateral shrinkage.

To further study the role of the boundary on crack formation, we reduced sample-boundary adhesion by coating the Petri dish with vacuum grease. These experiments, presented in Supplementary Information Fig. S9 and discussed in section ST2, show that reduction in sample-boundary adhesion promotes isotropic shrinkage and results in delayed cracking. For our subsequent studies on crack onset in drying clay suspension layers, we ensured maximum sample-boundary adhesion by loading samples in uncoated Petri dishes.

### 3.3. AFM microindentation measurements reveal an inverse correlation between crack onset time and sample elasticity

The onset of cracking in layers or sessile drops of colloidal suspensions depends on the elastic properties of the material [23] and the evaporation rate [72]. We performed microindentation experiments in an atomic force microscope to correlate the crack onset time,  $t_c$ , with the elasticity,  $E$ , of the drying clay suspension in a fully-developed gel state. For measuring meaningful force-indentation depth curves, we ensured that the samples tested were sufficiently elastic ( $E \geq 0.5$  MPa). Since clay samples with added TSPP do not have measurable elasticity and do not crack, these samples were excluded from further analysis. The inset of Fig. 4 shows representative force-indentation depth curves at elapsed time  $t = 14$  h for partially dried clay suspensions with different NaCl contents. The elasticity of each sample was extracted by fitting the data to the Hertz model, shown as solid black lines in the inset, using a protocol outlined in Supplementary Information Section ST1. Elasticity values thus estimated at  $t = 14$  h are plotted in Fig. 4.

$t_c$  and  $E$  values for all the samples are tabulated in Supplementary Information Table S10. Sample elasticity measurements corresponding to another elapsed time in the constant evaporation rate regime are presented in Supplementary Information Fig. S11(a).

Crack onset times,  $t_c$  are plotted vs. sample elasticity,  $E$ , in Fig. 5(a), for data acquired at elapsed time  $t = 14$  h. The error bars represent standard errors estimated from at least 3 independent measurements. The observed inverse correlation between  $t_c$  and  $E$  verifies that highly elastic samples crack earlier.

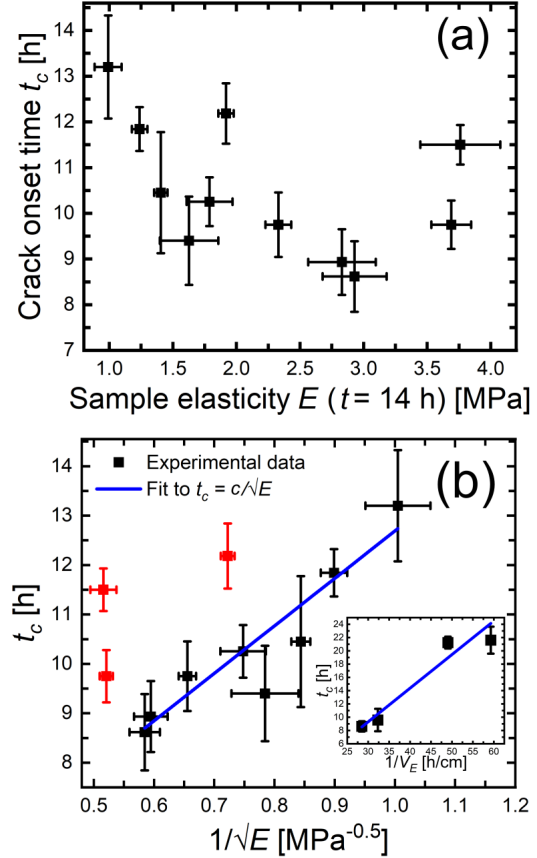


Figure 5: **Inverse correlation between crack onset time and sample elasticity.** (a) Crack onset time,  $t_c$ , vs. sample elasticity,  $E$ . (b) Crack onset time,  $t_c$ , vs. inverse square root of sample elasticity,  $\frac{1}{\sqrt{E}}$ . Apart from three data points (in red) that are expected to be driven into the nematic gel phase upon desiccation, all other points lie on a (blue) straight line. Horizontal and vertical error bars represent standard errors calculated from at least 3 measurements. (Inset) The variation of  $t_c$  with evaporation rate,  $V_E$ , of the drying sample. The blue line is a straight-line fit to this data.

### 3.4. Modelling the inverse correlation between crack onset time, $t_c$ , and sample elasticity, $E$

We model the observed variation of crack onset time,  $t_c$ , with sample elasticity,  $E$ , displayed in Fig. 5(a), by incorporating the Griffith's criterion for crack formation [8] in a one-dimensional poroelastic model [73]. In the context of our experiments wherein water diffuses through the microscopic pores of

the deformable clay gel during desiccation, the pressure distribution in the pores should satisfy the following diffusion equation [23, 47, 74, 75]:

$$\frac{\partial p}{\partial t} = \frac{\kappa E}{\eta} \frac{\partial^2 p}{\partial z^2} \quad (1)$$

In this equation,  $z = 0$  and  $z = h$  correspond to the bottom and top surfaces of the drying clay suspension respectively, with free evaporation allowed only at  $z = h$  as illustrated in Fig. 1(d). Furthermore,  $\frac{\kappa E}{\eta}$  is the consolidation coefficient, where  $\eta$  is the viscosity of water,  $E$  is the elasticity and  $\kappa$  is the permeability of the porous gel. As discussed in Supplementary Information section ST4, the permeability of our samples is estimated to be  $\approx 10^{-19} \text{m}^2$  using the Carman–Kozeny relationship [76]. Assuming  $\eta = 10^{-3} \text{Pa}\cdot\text{s}$  and  $E = 10^6 \text{Pa}$ , the consolidation coefficient  $\approx 10^{-10} \text{m}^2/\text{s}$ . The low value of the consolidation coefficient indicates an extremely slow rate of water diffusion through the pores of the gel and inadequate compensation for solvent loss at the free evaporation surface. In addition, capillary pressure at the surface is expected to remain high due to meniscus formation. These factors [2], along with constrained lateral shrinkage of the clay sample due to its adhesion with the Petri dish wall, result in the observed cracking.

The pressure  $p$  in the sample along the  $z$ -axis satisfies the following conditions [23]: (i)  $p(z, t = 0) = p_i$ , the atmospheric pressure at the start of desiccation at  $t = 0$ , (ii)  $\frac{\partial p}{\partial z} = 0$  for  $t > 0$  at  $z = 0$ , and (iii)  $\frac{\partial p}{\partial z} = -\frac{\eta V_E}{\kappa}$  at  $z = h$  due to solvent loss for an evaporation rate,  $V_E$ . The solution of Eqn. 1 under these conditions yields the pressure at the evaporating surface of the sample:  $p(z = h, t) \approx \frac{E V_E}{h} t + p_i$  [23, 77, 78]. The desiccation-induced stress generated at the free evaporating surface,  $z = h$ , is given by [23, 77]:

$$\sigma(h, t) = p(h, t) - p_i \approx \frac{E V_E}{h} t \quad (2)$$

According to Griffith's criterion for equilibrium crack propagation [8], the first crack develops at a critical cracking stress  $\sigma_c$  [6]:

$$\sigma_c = \sqrt{\frac{\mathcal{G}_c E}{\pi a}} \quad (3)$$

Here,  $\mathcal{G}_c$ , the fracture energy of the sample, is the total energy per unit area required for crack propagation and  $a$  is the crack length. Since for crack onset at  $t = t_c$ , the stress at the surface of the sample  $\sigma(h, t = t_c)$  must be equal to the critical cracking stress  $\sigma_c$ , we combine Eqns. 2 and 3 to obtain:

$$t_c \approx \left[ \sqrt{\frac{\mathcal{G}_c}{\pi a}} \frac{h}{V_E} \right] \sqrt{\frac{1}{E}} \quad (4)$$

Our simple model therefore predicts that crack onset time scales inversely with the square root of sample elasticity:  $t_c \propto \frac{1}{\sqrt{E}}$ . To check the validity of our model, we have re-plotted the data in Fig. 5(a) in the form  $t_c$  vs.  $1/\sqrt{E}$  in Fig. 5(b). Apart from three data points (marked in red) that correspond to samples with the highest clay and lowest salt concentrations, all other data points (marked in black) lie on a straight line as predicted

by our model. In Supplementary Information Fig. S12, we have reproduced a phase diagram for aqueous Laponite suspensions in the clay concentration - NaCl concentration plane [40]. The samples corresponding to the red data points in Fig. 5(b) lie in close proximity to the phase boundary at  $t = 0$  and are expected to evolve into directed nematic gel phases as the aging samples consolidate due to desiccation-induced solvent loss. The poroelastic model, which describes the deformation of saturated isotropic gels, is therefore not applicable to these samples.

We now turn our attention to the black data points in Fig. 5(b) that agree with our model prediction,  $t_c \propto \frac{1}{\sqrt{E}}$ . According to Eqn. 4, the slope of the blue straight line in Fig. 5(b) is  $\sqrt{\frac{\mathcal{G}_c}{\pi a}} \frac{h}{V_E}$ . Assuming  $h \approx a \approx 10^{-3} \text{m}$  and evaporation rate  $V_E = 10^{-7} \text{m/sec}$  at  $50^\circ\text{C}$ , the fracture energy  $\mathcal{G}_c \approx 10^3 \text{J/m}^2$ , which indicates that drying clay samples are highly ductile and deform significantly before the appearance of the first crack.

The predicted scaling between the crack onset time and sample elasticity was also verified by performing microindentation measurements at an elapsed time  $t = 15 \text{h}$ . A linear fit to the data, displayed in Supplementary Information Fig. S11(b), yields  $\mathcal{G}_c \approx 10^3 \text{J/m}^2$  and agrees very well with our previous estimate. Next, the crack onset time for drying suspensions of 3% w/v clay with 4 mM NaCl was recorded at different chamber temperatures and therefore at different evaporation rates,  $V_E$ . The data, presented in the inset of Fig. 5(b), satisfies  $t_c \propto 1/V_E$  as predicted by Eqn. 4, with  $\mathcal{G}_c \approx 10^3 \text{J/m}^2$ . The computation of  $V_E$  at different temperatures is displayed in Supplementary Information Fig. S13.

Our simplified one-dimensional theory can therefore be successfully employed to explain the complex cracking phenomenon in heterogeneous viscoelastic aging clay suspensions. Finally, Eqn. 4 is fitted to data extracted from Dauphiné and Pauchard's study [23] on crack onset during the drying of silica particle suspensions and presented in Supplementary Information Fig. S14. The observed linear relationship between  $t_c$  and  $1/\sqrt{E}$  indicates that our prediction of an inverse scaling relation between crack onset time and square root of sample elasticity can be successfully extended to desiccation crack onset in other gel-forming colloidal suspensions.

#### 4. Conclusions

Desiccation cracks [5] in drying soil or clay structures are driven by the development of evaporation-induced differential strains [6, 34, 35]. As the underlying clay suspension microstructures consolidate due to the combined effects of aging and desiccation, the ability of the sample to support large stresses and store strain energy improves considerably. While aging a gel prior to drying has been shown to reduce the risk of fracturing by strengthening the sample microstructures [44, 45, 46, 47], a systematic investigation of the combined effects of aging dynamics and solvent loss on the formation of desiccation cracks in drying samples has never been explored in the literature. In the present work, we experimentally studied the onset of cracking in desiccating clay suspension layers by first investigating the role of substrate adhesion.

Our digital image correlation analyses [69, 70] revealed that the generation of substantial differential strains in the presence of sample-boundary adhesion results in faster crack onset.

It was previously reported that static electric fields can rapidly accelerate the aging dynamics of aqueous Laponite clay suspensions [58], with cracks forming earlier when the static electric field strength was increased [63]. In our present study, we accelerated [49, 63] and inhibited [54] sample aging, and therefore sample solidification due to microstructural build-up [37, 38, 39], by incorporating sodium chloride (NaCl) and tetrasodium pyrophosphate (TSPP) respectively in the suspension medium. For maximal sample-boundary adhesion, direct imaging studies demonstrated that cracks formed earlier in drying clay suspensions with added NaCl, while the presence of TSPP fluidised the suspension and delayed crack formation. Furthermore, we showed *via* microindentation measurements [71] that clay suspensions with higher NaCl content are characterised by higher elasticity values due to the rapid formation of elastic clay gels.

Combining our microindentation results with our imaging data, we demonstrated that the crack onset time,  $t_c$ , is inversely correlated with the square root of sample elasticity,  $E$ , of the partially dried sample, *i.e.*  $t_c \propto 1/\sqrt{E}$ . We successfully modelled this correlation by incorporating the Griffith's criterion in a one-dimensional poroelasticity theory. We experimentally validated another model prediction,  $t_c \propto \frac{1}{V_E}$ , where  $V_E$  is the evaporation rate, by performing additional experiments at different environmental chamber temperatures. Fits of our model to our experimental datasets yielded fracture energy values of the order of  $10^3$  J/m<sup>2</sup> [6], indicating that desiccating clay suspensions undergo ductile fracturing and can sustain large deformations due to avalanches of localised plastic events before yielding or cracking [79]. This is reasonable, given the fragile nature [80] of clay gels. Finally, we analysed previously published data on the cracking of drying silica gel droplets [23] and verified an inverse correlation between crack onset time and the square root of sample elasticity. Our findings can therefore be extended to other desiccating systems.

One of the major shortcomings of our model is its applicability to only isotropic gel-forming materials. Deriving a correlation between crack onset time and mechanical modulus of an anisotropic gel, such as those expected to form at higher clay concentrations [40], would be an interesting future direction. We must also note that incorporating the temporal evolution of sample elasticity and film height in the poroelastic model would ensure a more accurate prediction of crack onset time. However, despite its limitations, it is indeed encouraging that our toy model can successfully capture several features of the complex desiccation process.

A deeper understanding of the cracking phenomenon is important in heritage science, for example, in detecting the authenticity of old paintings or in creating craquelure art. Since clays are biodegradable [81] and ubiquitous in various industrial products [82], our results are useful in the formulation of crack-resistant films, coatings [64], rheological modifiers, etc. The scaling relations between crack onset time, sample elasticity and evaporation rate, as unearthed by us in this study, can

be exploited to predict and prevent desiccation-induced cracking in natural clayey soils, clay pottery and other clay-based structures. Indeed, improved predictions of time and location of desiccation crack onset may be achieved by employing machine learning algorithms [83] for analysing strain fields on the surface of the desiccating sample. The location and risk of fracture could then be predicted with improved accuracy, thereby preventing catastrophic failure events.

## 5. CRediT authorship contribution statement

**VRS Parmar:** Methodology, Software, Writing - Original Draft, Validation, Formal analysis, Investigation, Writing - Review & Editing, Visualization. **RB:** Conceptualization, Supervision, Project administration, Writing - Original Draft, Visualization, Writing - Review & Editing, Funding acquisition, Resources.

## 6. Declaration of competing interest

The authors declare that they have no known competing financial interests or personal relationships that could have influenced the work reported in this paper.

## 7. Acknowledgement

The authors thank Yatheendran K. M. for help with AFM microindentation measurements, Shivprasad Patil for their expertise in microindentation technique, Lucas Goehring for their expertise on desiccation cracks and Abhishek gadhai for useful discussions related to digital image correlation experiments.

## References

- [1] L. Goehring, Evolving fracture patterns: columnar joints, mud cracks and polygonal terrain, *Philos. Trans. R. Soc. A* 371 (2004) (2013) 20120353. doi:10.1098/rsta.2012.0353.
- [2] G. W. Scherer, Stress and fracture during drying of gels, *J. Non-Cryst. Solids* 121 (1) (1990) 104–109, proceedings of the Fifth International Workshop on Glasses and Ceramics from Gels. doi:10.1016/0022-3093(90)90113-Z.
- [3] S. Kitsunozaki, Crack growth in drying paste, *Adv. Powder Technol.* 22 (3) (2011) 311–318. doi:10.1016/j.apt.2011.03.006.
- [4] A. F. Routh, Drying of thin colloidal films, *Rep. Prog. Phys.* 76 (4) (2013) 046603. doi:10.1088/0034-4885/76/4/046603.
- [5] R. Mondal, H. Lama, K. C. Sahu, Physics of drying complex fluid drop: Flow field, pattern formation, and desiccation cracks, *Phys. Fluids* 35 (6) (2023) 061301. doi:10.1063/5.0153682.
- [6] L. Goehring, A. Nakahara, T. Dutta, S. Kitsunozaki, S. Tarafdar, *Desiccation Cracks and their Patterns*, John Wiley & Sons, Ltd, 2015. doi:10.1002/9783527671922.
- [7] S. Bohn, L. Pauchard, Y. Couder, Hierarchical crack pattern as formed by successive domain divisions., *Phys. Rev. E* 71 (2005) 046214. doi:10.1103/PhysRevE.71.046214.
- [8] A. A. Griffith, The Phenomena of Rupture and Flow in Solids, *Philos. Trans. R. Soc. A* 221 (1921) 163–198. doi:10.1098/rsta.1921.0006.
- [9] A. Groisman, E. Kaplan, An experimental study of cracking induced by desiccation, *EPL* 25 (6) (1994) 415. doi:10.1209/0295-5075/25/6/004.

- [10] L. Goehring, R. Conroy, A. Akhter, W. J. Clegg, A. F. Routh, Evolution of mud-crack patterns during repeated drying cycles, *Soft Matter* 6 (2010) 3562–3567. doi:10.1039/B922206E.
- [11] T. Boeck, H.-A. Bahr, S. Lampenscherf, U. Bahr, Self-driven propagation of crack arrays: A stationary two-dimensional model, *Phys. Rev. E* 59 (1999) 1408–1416. doi:10.1103/PhysRevE.59.1408.
- [12] F. Giorgiutti-Dauphiné, L. Pauchard, Painting cracks: A way to investigate the pictorial matter, *J. Appl. Phys.* 120 (6) (2016) 065107. doi:10.1063/1.4960438.
- [13] J. G. McGrath, R. D. Bock, J. M. Cathcart, L. A. Lyon, Self-Assembly of “Paint-On” Colloidal Crystals Using Poly(styrene-co-N-isopropylacrylamide) Spheres, *Chem. Mater.* 19 (7) (2007) 1584–1591. doi:10.1021/cm061931y.
- [14] M. C. Milinkovitch, L. Manukyan, A. Debry, N. Di-Poï, S. Martin, D. Singh, D. Lambert, M. Zwicker, Crocodile Head Scales Are Not Developmental Units But Emerge from Physical Cracking, *Science* 339 (6115) (2013) 78–81. doi:10.1126/science.1226265.
- [15] L. Goehring, L. Mahadevan, S. W. Morris, Nonequilibrium scale selection mechanism for columnar jointing, *PNAS* 106 (2) (2009) 387–392. doi:10.1073/pnas.0805132106.
- [16] R. Weinberger, Evolution of polygonal patterns in stratified mud during desiccation: The role of flaw distribution and layer boundaries, *GSA Bulletin* 113 (1) (2001) 20–31. doi:10.1130/0016-7606(2001)113<0020:EOPPIS>2.0.CO;2.
- [17] D. Brutin, B. Sobac, C. Nicloux, Influence of Substrate Nature on the Evaporation of a Sessile Drop of Blood, *J. Heat Transf.* 134 (6) (2012) 061101. doi:10.1115/1.4006033.
- [18] N. Laan, F. Smith, C. Nicloux, D. Brutin, Morphology of drying blood pools, *Forensic Sci. Int.* 267 (2016) 104–109. doi:10.1016/j.forsciint.2016.08.005.
- [19] J. C. Flores, Mean-field crack networks on desiccated films and their applications: Girl with a pearl earring, *Soft Matter* 13 (2017) 1352–1356. doi:10.1039/C6SM02849G.
- [20] A. Nakahara, Y. Matsuo, Transition in the pattern of cracks resulting from memory effects in paste, *Phys. Rev. E* 74 (2006) 045102. doi:10.1103/PhysRevE.74.045102.
- [21] C.-S. Tang, Y.-J. Cui, A.-M. Tang, B. Shi, Experiment evidence on the temperature dependence of desiccation cracking behavior of clayey soils, *Eng. Geol.* 114 (3) (2010) 261–266. doi:10.1016/j.enggeo.2010.05.003.
- [22] W. Meng, M. Liu, Y. Gan, L. Pauchard, C. Q. Chen, Cracking to curling transition in drying colloidal films, *Eur. Phys. J. E* 43 (10) (2020) 64. doi:10.1140/epje/i2020-11985-4.
- [23] F. Giorgiutti-Dauphiné, L. Pauchard, Elapsed time for crack formation during drying, *Eur. Phys. J. E* 37 (5) (2014) 39. doi:10.1140/epje/i2014-14039-8.
- [24] L. Pauchard, F. Parisse, C. Allain, Influence of salt content on crack patterns formed through colloidal suspension desiccation, *Phys. Rev. E* 59 (1999) 3737–3740. doi:10.1103/PhysRevE.59.3737.
- [25] M. S. Tirumkudulu, W. B. Russel, Cracking in Drying Latex Films, *Langmuir* 21 (11) (2005) 4938–4948. doi:10.1021/la048298k.
- [26] H. Lama, M. G. Basavaraj, D. K. Satapathy, Desiccation cracks in dispersion of ellipsoids: Effect of aspect ratio and applied fields, *Phys. Rev. Mater.* 2 (2018) 085602. doi:10.1103/PhysRevMaterials.2.085602.
- [27] S. Kumar, M. G. Basavaraj, D. K. Satapathy, Effect of Colloidal Surface Charge on Desiccation Cracks, *Langmuir* 39 (29) (2023) 10249–10258. doi:10.1021/acs.langmuir.3c01326.
- [28] K. B. Singh, M. S. Tirumkudulu, Cracking in Drying Colloidal Films, *Phys. Rev. Lett.* 98 (2007) 218302. doi:10.1103/PhysRevLett.98.218302.
- [29] E. Santanach Carreras, F. Chabert, D. Dunstan, G. Franks, Avoiding “mud” cracks during drying of thin films from aqueous colloidal suspensions, *J. Colloid Interface Sci.* 313 (1) (2007) 160–168. doi:10.1016/j.jcis.2007.03.076.
- [30] J. Thiery, E. Keita, S. Rodts, D. Courtier Murias, T. Kodger, A. Pegoraro, P. Coussot, Drying kinetics of deformable and cracking nanoporous gels, *Eur. Phys. J. E* 39 (12) (2016) 117. doi:10.1140/epje/i2016-16117-3.
- [31] A. W. Zaibudeen, R. Bandyopadhyay, DC field coupled evaporation of a sessile gold nanofluid droplet, *Soft Matter* 17 (2021) 10294–10300. doi:10.1039/D1SM00820J.
- [32] H. Lama, T. Gogoi, M. G. Basavaraj, L. Pauchard, D. K. Satapathy, Synergy between the crack pattern and substrate elasticity in colloidal deposits, *Phys. Rev. E* 103 (2021) 032602. doi:10.1103/PhysRevE.103.032602.
- [33] S. Kumar, M. G. Basavaraj, D. K. Satapathy, Effect of the Shape of the Confining Boundary and Particle Shape Anisotropy on the Morphology of Desiccation Cracks, *Langmuir* 38 (26) (2022) 7906–7913. doi:10.1021/acs.langmuir.2c00197.
- [34] C.-S. Tang, C. Zhu, Q. Cheng, H. Zeng, J.-J. Xu, B.-G. Tian, B. Shi, Desiccation cracking of soils: A review of investigation approaches, underlying mechanisms, and influencing factors, *Earth-Sci. Rev.* 216 (2021) 103586. doi:10.1016/j.earscirev.2021.103586.
- [35] S. Tarafdar, S. Sinha, Crack Formation in Drying Laponite, *Ind. Eng. Chem. Res.* 47 (17) (2008) 6459–6464. doi:10.1021/ie071375x.
- [36] H. Van Olphen, *An Introduction to Clay Colloid Chemistry: For Clay Technologists, Geologists and Soil Scientists*. 2nd edition, Wiley, New York, 1977.
- [37] R. Bandyopadhyay, D. Liang, H. Yardimci, D. A. Sessoms, M. A. Borthwick, S. G. J. Mochrie, J. L. Harden, R. L. Leheny, Evolution of Particle-Scale Dynamics in an Aging Clay Suspension, *Phys. Rev. Lett.* 93 (2004) 228302. doi:10.1103/PhysRevLett.93.228302.
- [38] B. Abou, D. Bonn, J. Meunier, Aging dynamics in a colloidal glass, *Phys. Rev. E* 64 (2001) 021510. doi:10.1103/PhysRevE.64.021510.
- [39] A. Knaebel, M. Bellour, J.-P. Munch, V. Viasnoff, F. Lequeux, J. L. Harden, Aging behavior of Laponite clay particle suspensions, *EPL* 52 (1) (2000) 73. doi:10.1209/epl/i2000-00406-6.
- [40] K. Suman, Y. M. Joshi, Microstructure and Soft Glassy Dynamics of an Aqueous Laponite Dispersion, *Langmuir* 34 (44) (2018) 13079–13103. doi:10.1021/acs.langmuir.8b01830.
- [41] L. Cipelletti, S. Manley, R. C. Ball, D. A. Weitz, Universal aging features in the restructuring of fractal colloidal gels, *Phys. Rev. Lett.* 84 (2000) 2275–2278. doi:10.1103/PhysRevLett.84.2275.
- [42] H. Yardimci, R. L. Leheny, Memory in an aging molecular glass, *EPL* 62 (2) (2003) 203. doi:10.1209/epl/i2003-00347-0.
- [43] L. C. E. Struik, et al., *Physical aging in amorphous polymers and other materials*, Vol. 106, Citeseer, 1978.
- [44] J. Zarzycki, M. Prassas, J. Phalippou, Synthesis of glasses from gels: the problem of monolithic gels, *J. Mater. Sci.* 17 (11) (1982) 3371–3379. doi:10.1007/BF01203507.
- [45] U. K. H. Bangi, A. Venkateswara Rao, A. Parvathy Rao, A new route for preparation of sodium-silicate-based hydrophobic silica aerogels via ambient-pressure drying, *Sci Technol Adv Mater* 9 (3) (2008) 035006. doi:10.1088/1468-6996/9/3/035006.
- [46] J. Estella, J. C. Echeverría, M. Laguna, J. J. Garrido, Effects of aging and drying conditions on the structural and textural properties of silica gels, *Microporous Mesoporous Mater.* 102 (1) (2007) 274–282. doi:10.1016/j.micromeso.2007.01.007.
- [47] C. J. Brinker, G. W. Scherer, CHAPTER 8 - Drying, in: C. J. Brinker, G. W. Scherer (Eds.), *Sol-Gel Science*, Academic Press, San Diego, 1990, pp. 452–513. doi:10.1016/B978-0-08-057103-4.50013-1.
- [48] B. Ruzicka, E. Zaccarelli, A fresh look at the Laponite phase diagram, *Soft Matter* 7 (2011) 1268–1286. doi:10.1039/C0SM00590H.
- [49] D. Saha, R. Bandyopadhyay, Y. M. Joshi, Dynamic Light Scattering Study and DLVO Analysis of Physicochemical Interactions in Colloidal Suspensions of Charged Disks, *Langmuir* 31 (10) (2015) 3012–3020. doi:10.1021/acs.langmuir.5b00291.
- [50] S. Ali, R. Bandyopadhyay, Evaluation of the exfoliation and stability of na-montmorillonite in aqueous dispersions, *Appl. Clay Sci.* 114 (2015) 85–92. doi:10.1016/j.clay.2015.05.013.
- [51] S. L. Tawari, D. L. Koch, C. Cohen, Electrical Double-Layer Effects on the Brownian Diffusivity and Aggregation Rate of Laponite Clay Particles, *J. Colloid Interface Sci.* 240 (1) (2001) 54–66. doi:10.1006/jcis.2001.7646.
- [52] M. Delhorme, B. Jönsson, C. Labbez, Monte carlo simulations of a clay inspired model suspension: the role of rim charge, *Soft Matter* 8 (2012) 9691–9704. doi:10.1039/C2SM25731A.
- [53] R. Biswas, V. R. S. Parmar, A. G. Thambi, R. Bandyopadhyay, Correlating microscopic viscoelasticity and structure of an aging colloidal gel using active microrheology and cryogenic scanning electron microscopy, *Soft Matter* 19 (2023) 2407–2416. doi:10.1039/D2SM01457B.

- [54] C. Martin, F. Pignon, J.-M. Piau, A. Magnin, P. Lindner, B. Cabane, Dissociation of thixotropic clay gels, *Phys. Rev. E* 66 (2002) 021401. doi:10.1103/PhysRevE.66.021401.
- [55] K. Suman, M. Mittal, Y. M. Joshi, Effect of sodium pyrophosphate and understanding microstructure of aqueous LAPONITE® dispersion using dissolution study, *J. Phys. Condens. Matter* 32 (22) (2020) 224002. doi:10.1088/1361-648X/ab724d.
- [56] V. Thrithamara Ranganathan, R. Bandyopadhyay, Effects of aging on the yielding behaviour of acid and salt induced Laponite gels, *Colloids Surf. A* 522 (2017) 304–309. doi:10.1016/j.colsurfa.2017.03.006.
- [57] C. Misra, V. T. Ranganathan, R. Bandyopadhyay, Influence of medium structure on the physicochemical properties of aging colloidal dispersions investigated using the synthetic clay LAPONITE, *Soft Matter* 17 (2021) 9387–9398. doi:10.1039/D1SM00987G.
- [58] P. Gadige, R. Bandyopadhyay, Electric field induced gelation in aqueous nanoclay suspensions, *Soft Matter* 14 (2018) 6974–6982. doi:10.1039/C8SM00533H.
- [59] Y. Tan, R. Wu, H. Li, W. Ren, J. Du, S. Xu, J. Wang, Electric field-induced gradient strength in nanocomposite hydrogel through gradient crosslinking of clay, *J. Mater. Chem. B* 3 (2015) 4426–4430. doi:10.1039/C5TB00506J.
- [60] K. P. S. Parmar, Y. Méheust, B. Schjelderupsen, J. O. Fossum, Electrorheological Suspensions of Laponite in Oil: Rheometry Studies, *Langmuir* 24 (5) (2008) 1814–1822. doi:10.1021/1a702989u.
- [61] S. Nag, S. Sinha, S. Sadhukhan, T. Dutta, S. Tarafdar, Crack patterns in desiccating clay–polymer mixtures with varying composition, *J. Phys. Condens. Matter* 22 (1) (2009) 015402. doi:10.1088/0953-8984/22/1/015402.
- [62] T. Khatun, M. D. Choudhury, T. Dutta, S. Tarafdar, Electric-field-induced crack patterns: Experiments and simulation, *Phys. Rev. E* 86 (2012) 016114. doi:10.1103/PhysRevE.86.016114.
- [63] S. Tarafdar, T. Dutta, Formation of desiccation crack patterns in electric fields: a review, *Philos. Trans. R. Soc. A* 377 (2136) (2019) 20170398. doi:10.1098/rsta.2017.0398.
- [64] E. Huttunen-Saarivirta, G. Vaganov, V. Yudin, J. Vuorinen, Characterization and corrosion protection properties of epoxy powder coatings containing nanoclays, *Prog. Org. Coat.* 76 (4) (2013) 757–767. doi:10.1016/j.porgcoat.2013.01.005.
- [65] L. Greenspan, Humidity fixed points of binary saturated aqueous solutions, *J. Res. Natl. Bur. Stand. A Phys. Chem.* 81A (1) (1977) 89. doi:10.6028/jres.081A.011.
- [66] K. F. DeCarlo, N. Shokri, Effects of substrate on cracking patterns and dynamics in desiccating clay layers, *Water Resour. Res.* 50 (4) (2014) 3039–3051. doi:10.1002/2013WR014466.
- [67] P. Coussot, Scaling approach of the convective drying of a porous medium, *Eur. Phys. J. B* 15 (3) (2000) 557–566. doi:10.1007/s100510051160.
- [68] D. Tran, N. Ralaizafisoarivony, R. Charlier, B. Mercatoris, A. Léonard, D. Toye, A. Degré, Studying the effect of desiccation cracking on the evaporation process of a luvisol – from a small-scale experimental and numerical approach, *Soil Tillage Res.* 193 (2019) 142–152. doi:https://doi.org/10.1016/j.still.2019.05.018.
- [69] J. Blaber, B. Adair, A. Antoniou, Ncorr: Open-source 2d digital image correlation matlab software, *Exp. Mech.* 55 (6) (2015) 1105–1122. doi:10.1007/s11340-015-0009-1.
- [70] DIC Algorithms, <https://ncorr.com/index.php/dic-algorithms>, accessed: 2024-02-25.
- [71] N. Gavara, Combined strategies for optimal detection of the contact point in AFM force-indentation curves obtained on thin samples and adherent cells, *Sci. Rep.* 6 (1) (2016) 21267. doi:10.1038/srep21267.
- [72] M. Léang, F. Giorgiutti-Dauphiné, L.-T. Lee, L. Pauchard, Crack opening: from colloidal systems to paintings, *Soft Matter* 13 (2017) 5802–5808. doi:10.1039/C7SM00985B.
- [73] M. Biot, General theory of three-dimensional consolidation, *J. Appl. Phys.* 12 (1941) 155–164. doi:10.1063/1.1712886.
- [74] G. W. Scherer, Drying gels V. Rigid gels, *J. Non-Cryst. Solids* 92 (1) (1987) 122–144. doi:10.1016/S0022-3093(87)80364-2.
- [75] F. Giorgiutti-Dauphiné, L. Pauchard, Drying drops, *Eur. Phys. J. E* 41 (3) (2018) 32. doi:10.1140/epje/i2018-11639-2.
- [76] B. Kruczek, Carman–Kozeny Equation, Springer Berlin Heidelberg, Berlin, Heidelberg, 2015, pp. 1–3. doi:10.1007/978-3-642-40872-4\_1995-1}.
- [77] M. Chekchaki, V. Lazarus, Mechanical Stresses Induced by Evaporation in Consolidated Colloidal Suspensions of Hard Particles. Poroelasticity Theory Versus Experiments, *Transp. Porous Media* 100 (1) (2013) 143–157. doi:10.1007/s11242-013-0209-z.
- [78] G. W. Scherer, Drying gels: VIII. Revision and review, *J. Non-Cryst. Solids* 109 (2) (1989) 171–182. doi:10.1016/0022-3093(89)90029-X.
- [79] H. J. Barlow, J. O. Cochran, S. M. Fielding, Ductile and Brittle Yielding in Thermal and Athermal Amorphous Materials, *Phys. Rev. Lett.* 125 (2020) 168003. doi:10.1103/PhysRevLett.125.168003.
- [80] D. Saha, Y. M. Joshi, R. Bandyopadhyay, Kinetics of the glass transition of fragile soft colloidal suspensions, *J. Chem. Phys.* 143 (21) (2015) 214901. doi:10.1063/1.4936625.
- [81] S. Sharifi, S. B. Blanquer, T. G. van Kooten, D. W. Grijpma, Biodegradable nanocomposite hydrogel structures with enhanced mechanical properties prepared by photo-crosslinking solutions of poly(trimethylene carbonate)–poly(ethylene glycol)–poly(trimethylene carbonate) macromonomers and nanoclay particles, *Acta Biomater.* 8 (12) (2012) 4233–4243. doi:10.1016/j.actbio.2012.09.014.
- [82] J. L. Dávila, M. A. d’Ávila, Laponite as a rheology modifier of alginate solutions: Physical gelation and aging evolution, *Carbohydr. Polym.* 157 (2017) 1–8. doi:10.1016/j.carbpol.2016.09.057.
- [83] S. Boukhtache, K. Abdelouhab, F. Berry, B. Blaysat, M. Grédiac, F. Sur, When deep learning meets digital image correlation, *Opt. Lasers Eng.* 136 (2021) 106308. doi:https://doi.org/10.1016/j.optlaseng.2020.106308.

## Supplementary Information

# Tuning and predicting the onset of desiccation cracks in air-dried aqueous clay suspensions

Vaibhav Raj Singh Parmar<sup>1, †</sup> and Ranjini Bandyopadhyay<sup>1, \*</sup>

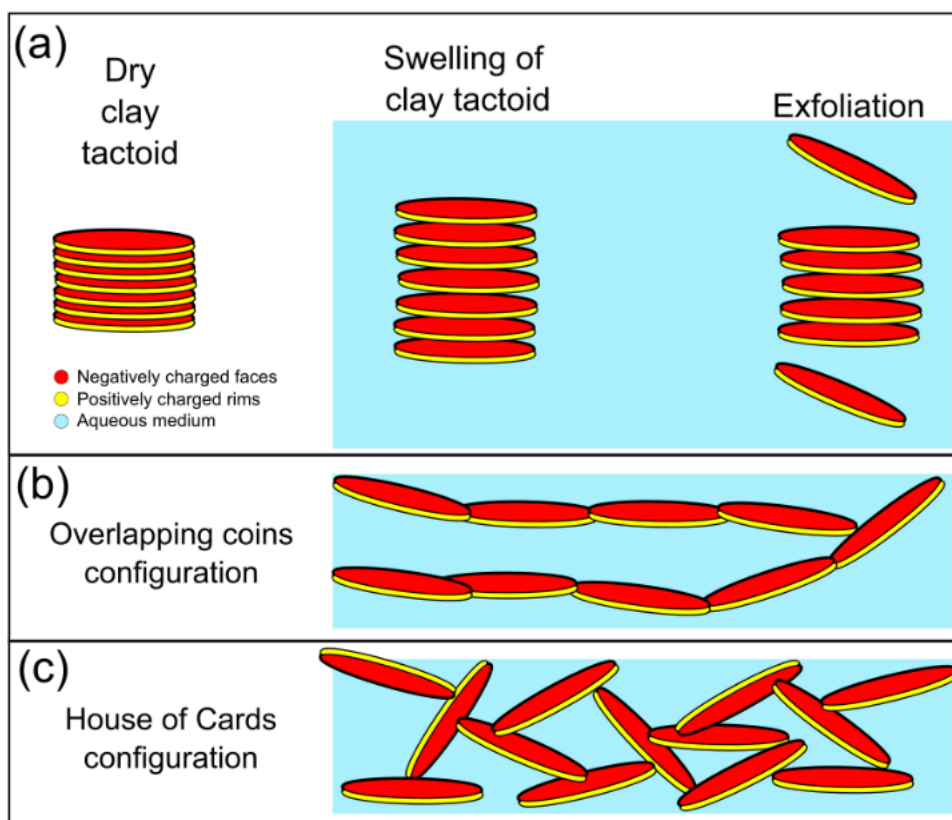
<sup>1</sup>*Soft Condensed Matter Group, Raman Research Institute, C. V. Raman Avenue,  
Sadashivanagar, Bangalore 560 080, INDIA*

July 2, 2024

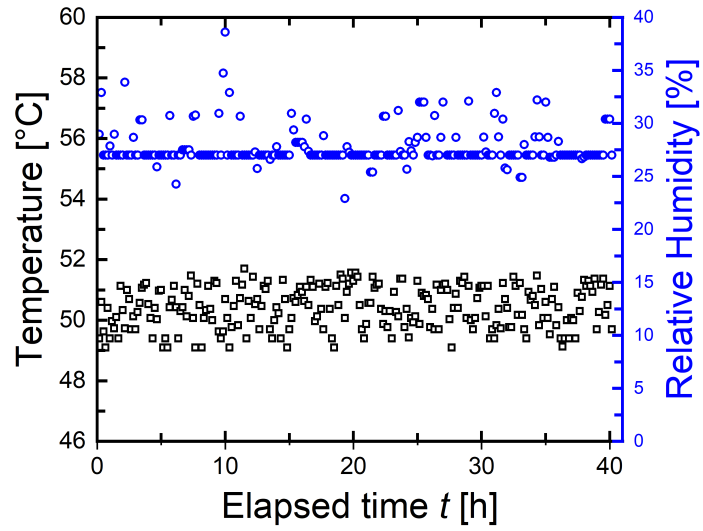
---

<sup>†</sup>vaibhav@rri.res.in

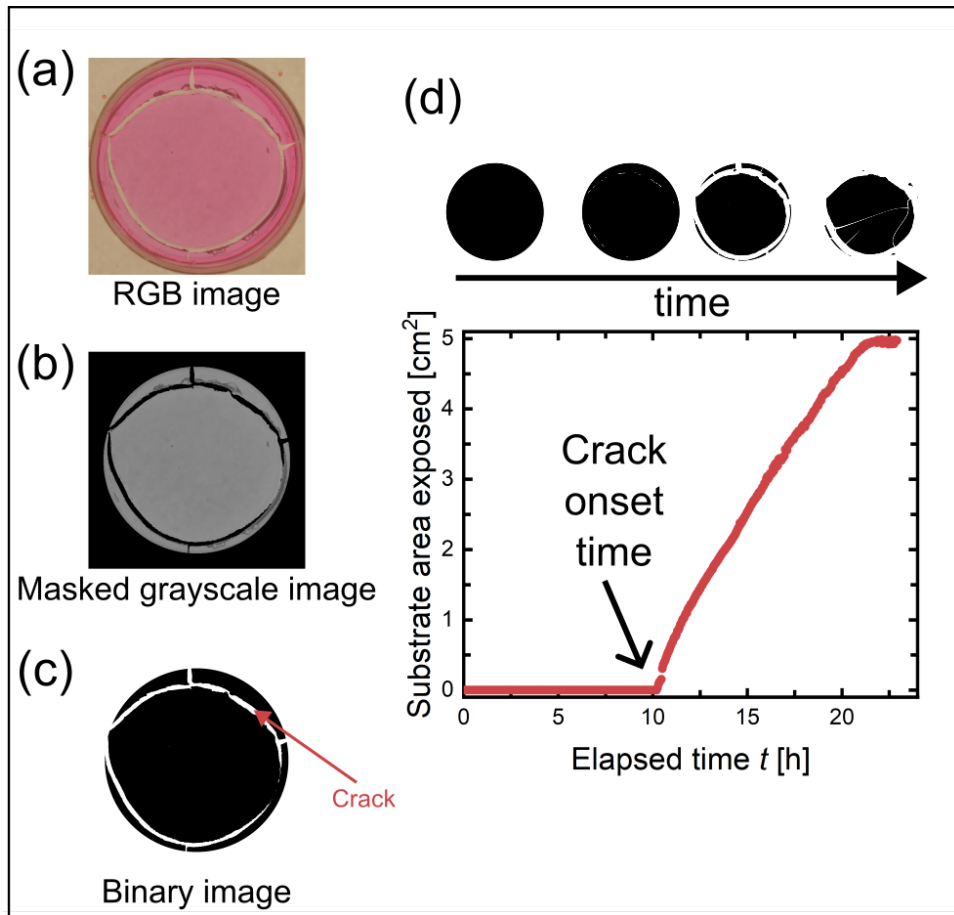
<sup>\*</sup>Corresponding Author: Ranjini Bandyopadhyay; Email: ranjini@rri.res.in



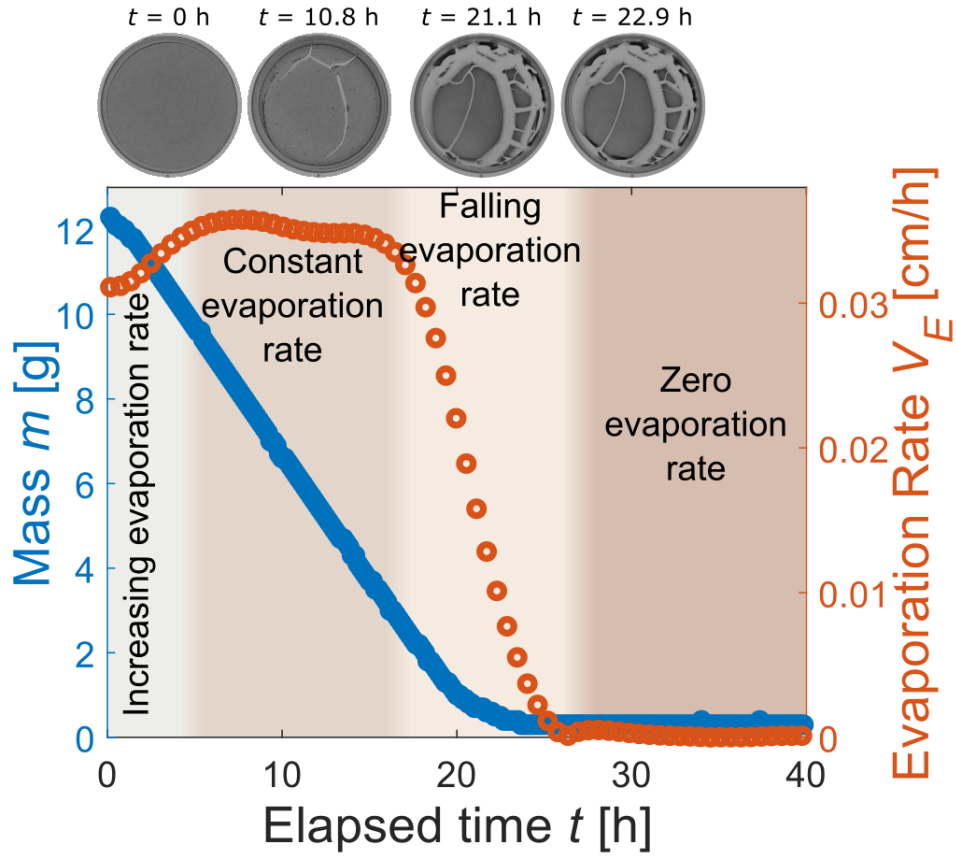
Supplementary Fig. S1: (a) Schematic illustration of the swelling and exfoliation of one-dimensional stacks (tactoids) of clay particles. Clay particles, in an aqueous medium acquire negative charges on the faces and positive charges on the rims and can self-assemble into (b) overlapping coin and (c) house of cards configurations as the concentration of salt in the medium decreases.



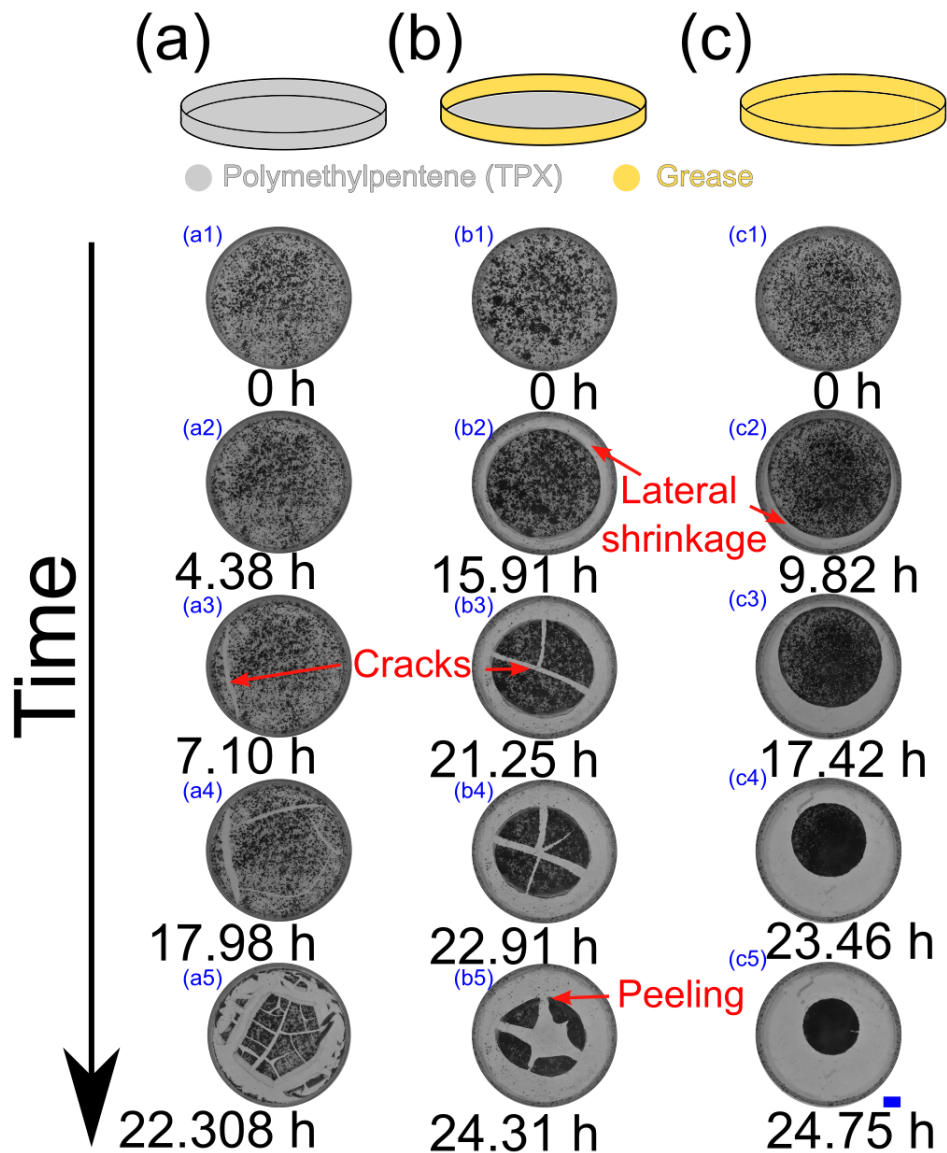
Supplementary Fig. S2: Temperature (left y-axis, black) and relative humidity (right y-axis, blue), measured using a DHT11 humidity and temperature sensor, were maintained at nearly constant values inside the experimental setup (Fig. 1(c)) for the entire experimental duration.



Supplementary Fig. S3: (a) A representative raw RGB image (top view) of a drying clay suspension. Rhodamine B was mixed to the suspension to ensure good contrast between the sample and substrate. (b) Masked and grayscale image, processed using K-means clustering based image segmentation [1]. (c) Binary image obtained from the grayscale image after setting an appropriate intensity threshold. (d) The substrate area exposed due to the formation of cracks is estimated from the binary image by counting the number of visible (white) pixels (pixel area =  $324 \mu\text{m}^2$ ). The top panel in (d) shows the progressive increase in the number of white pixels (and therefore, the exposed surface area) due to crack propagation. The substrate area exposed *vs.* elapsed time is plotted in the bottom panel. The elapsed time at which the exposed substrate area first becomes non-zero is designated as the crack onset time,  $t_c$ .



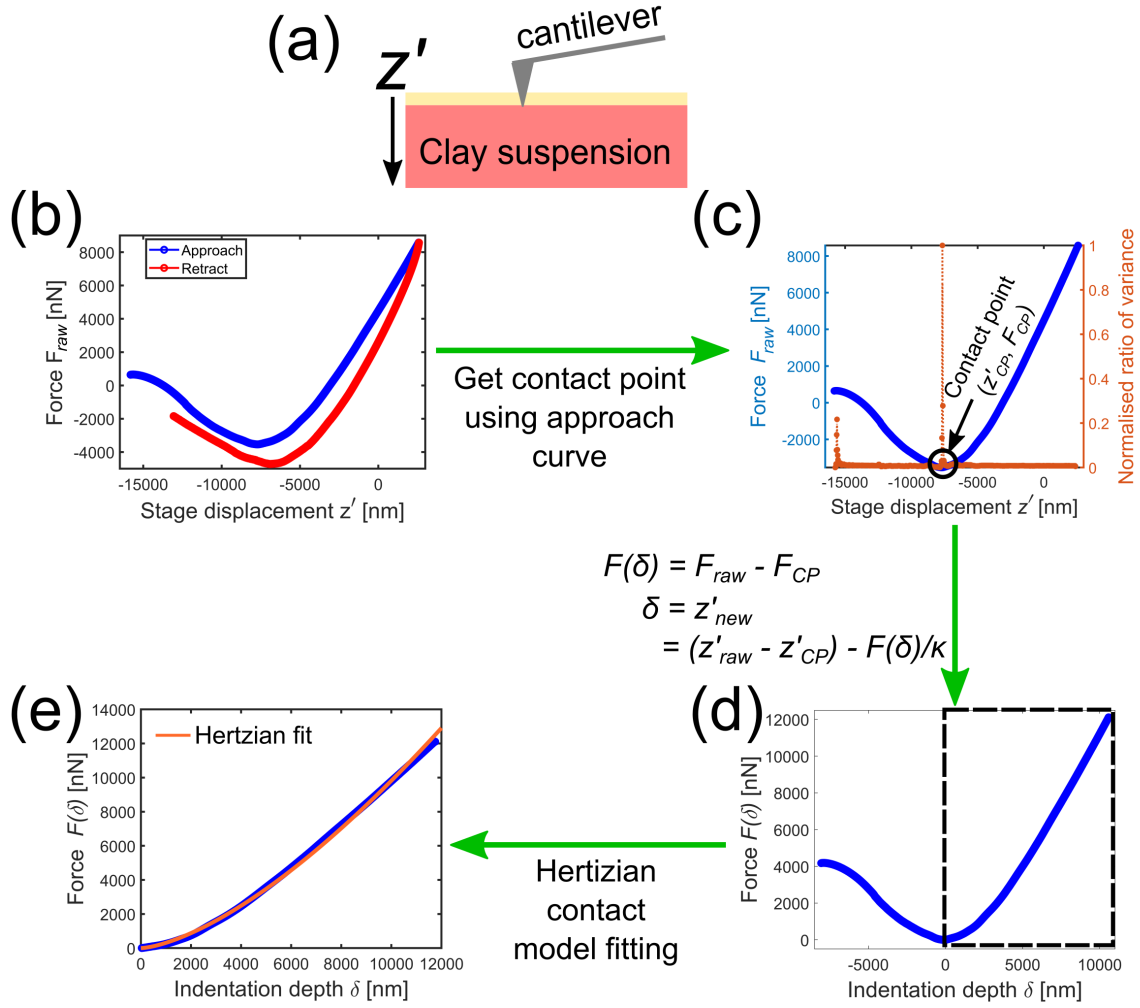
Supplementary Fig. S4: The top panel displays grayscale images showing the onset and propagation of cracks in drying clay suspensions. Mass  $m$  (left y-axis, blue) of the drying sample and the corresponding evaporation rate  $V_E$  (right y-axis, orange) as a function of elapsed time  $t$ . The evaporation rate shows an initial increase as the suspension, prepared at room temperature, equilibrates to the chamber temperature ( $T = 50^\circ\text{C}$ ). This is followed by a constant evaporation rate regime where the first crack is seen to form in all the samples studied in this work. Next, a rapid decrease in evaporation rate is seen. The final zero evaporation rate regime indicates a completely dried sample.



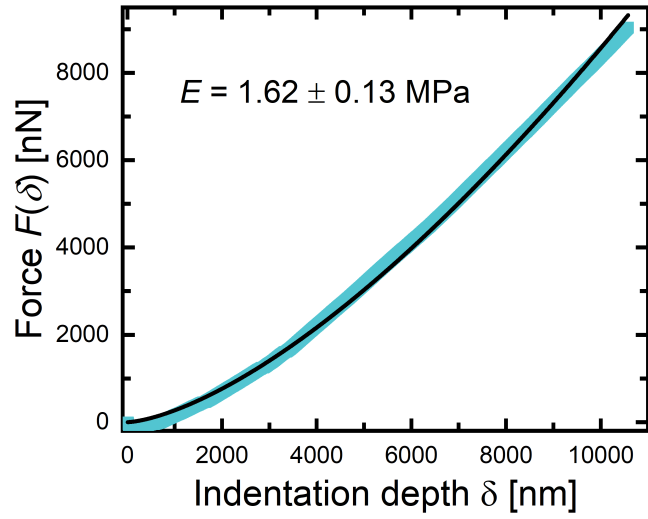
Supplementary Fig. S5: Fine pepper powder was sprinkled on the evaporating surface of clay samples, and strain fields were estimated by comparing subsequent images using digital image correlation analysis. The scale bar at the bottom right of (c5) is 6 mm. Grayscale images of a drying Laponite clay suspension of concentration 3.0% w/v with 4mM NaCl when **(a1-a5)** the sample adheres to both vertical boundary and bottom substrate, **(b1-b5)** the sample only adheres to the bottom substrate due to vacuum grease coating on the inner vertical boundary and **(c1-c5)** adhesion of the sample with vertical boundary and bottom substrate is removed by applying vacuum grease on all inner surfaces of the Petri dish. Clearly, cracking is most prominent when sample-boundary adhesion is maximum (a1-a5). In contrast, the sample shrinks but does not crack in the absence of adhesion (c1-c5).

## ST1 Microindentation measurements

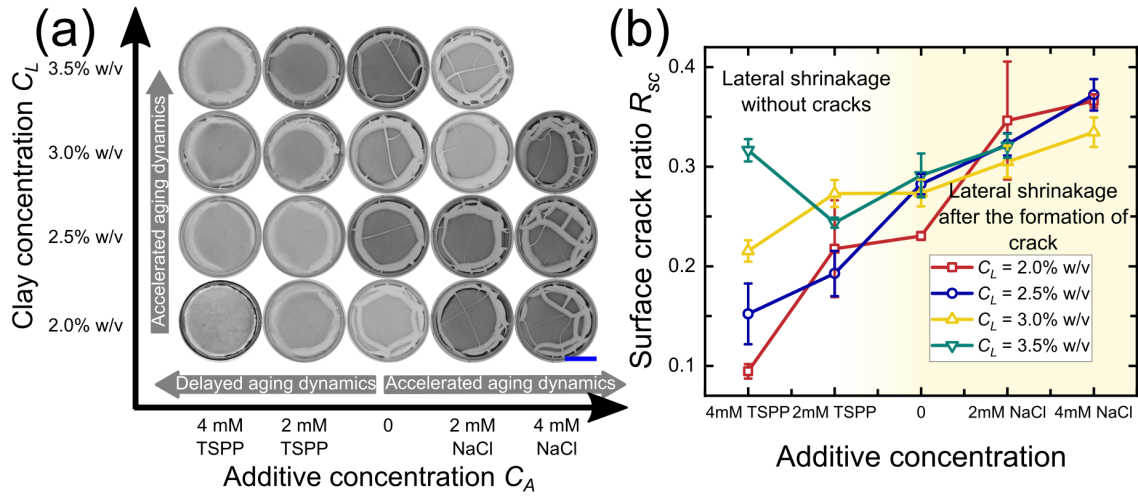
Sample elasticity was evaluated from force  $F(\delta)$  vs. indentation depth  $\delta$  curves, obtained using a microindentation technique in an atomic force microscope (AFM). The AFM cantilever tip approaches the clay sample through a layer of oil and indents the sample in contact mode. The cantilever-sample contact point in the force-indentation depth curve was determined using the ratio of variance method [2]. The force values were re-scaled as  $F(\delta) = F_{raw} - F_{CP}$ , where  $F_{raw}$  is the raw value of the force on the cantilever,  $F_{CP}$  is the force on the cantilever at the contact point. The stage displacement,  $z'$ , includes contributions from both cantilever deflection,  $F(\delta)/\kappa$  from Hooke's law, and sample indentation. The actual indentation depth,  $\delta$ , was determined from the stage displacement  $z'$  by using  $\delta = z' - z'_{CP} - F(\delta)/\kappa$  [3], where  $z'_{CP}$  is the stage displacement at the contact point.



Supplementary Fig. S6: (a) Schematic illustration of the cantilever approaching the clay suspension through a layer of oil. The cantilever moves in the direction  $\hat{z}' = -\hat{z}$  as indicated by the black arrow. (b) Raw force values  $F_{raw}$  are obtained from microindentation measurements as a function of stage displacement during cantilever approach and retraction. (c) The approaching part of the force-distance curve (left y-axis, blue) is plotted vs. stage displacement and the normalised ratio of variance [2] (right y-axis, red) was estimated to determine the contact point (CP). The ratio of variance is maximum at the contact point. (d) The experimental data is scaled to ensure zero force at the contact point. The indentation depth  $\delta$  is determined by subtracting cantilever deflection,  $F(\delta)/\kappa$ , from the cantilever stage displacement,  $(z' - z_{CP}')$ . (e) The rescaled  $F(\delta)$  vs.  $\delta$  curve for  $\delta \geq 0$  (shown within a dashed box in (d)) is fitted with the Hertzian contact model for a spherical tip to extract sample elasticity.

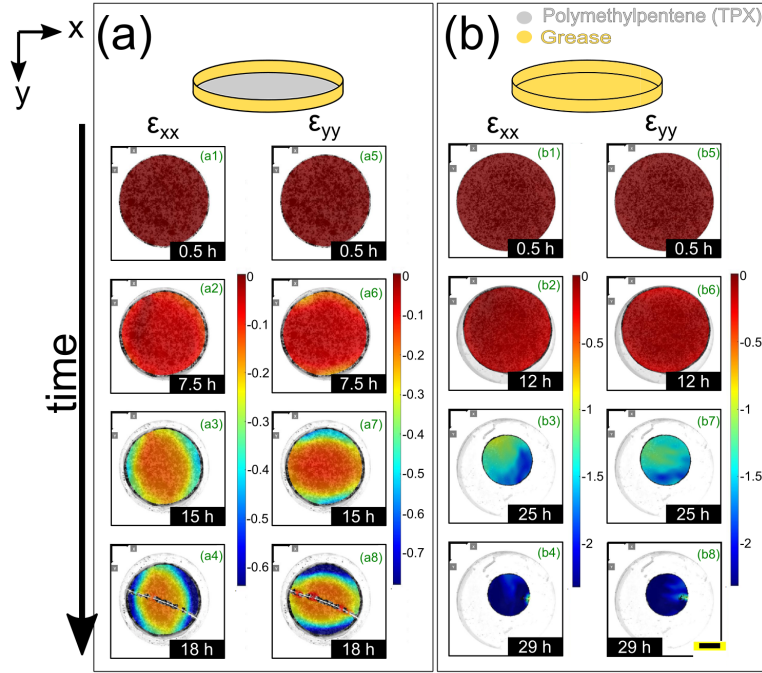


Supplementary Fig. S7: Force-indentation depth curve computed from the approach cycle of a microindentation experiment using a PDMS elastomer sample with base elastomer:crosslinking agent = 10:1 (by weight). Using the microindentation analysis protocol described earlier, the elasticity of the sample is found to be  $1.62 \pm 0.13$  MPa, in agreement with a previous estimate [4].



Supplementary Fig. S8: Crack patterns after completion of drying for samples with different clay and additive concentrations. Samples with low clay concentrations or with added TSPP show delayed aging dynamics and are less likely to crack, while samples with high NaCl content show accelerated aging dynamics and a dense network of cracks. The scale bar at the bottom right is 2 cm. **(b)** Surface crack ratio, defined as the fraction of total substrate area exposed due to sample cracking and/or shrinkage after desiccation is complete, is plotted *vs.* additive concentration. The error bars represent standard errors calculated from 3-4 experiments.

## ST2 Role of sample-boundary adhesion on crack formation



Supplementary Fig. S9: The temporal evolution of strain fields  $\epsilon_{xx}$  and  $\epsilon_{yy}$  in drying samples *vs.* elapsed time, when **(a1-a8)** only the inner rim of the Petri dish was coated with vacuum grease such that the sample adheres only to the bottom substrate, **(b1-b8)** vacuum grease was coated on all the inner surfaces of the Petri dish to minimise adhesion between the sample and all the Petri dish surfaces. The positive and negative values of strains in the colour bars indicate elongative and compressive strains respectively. Time stamps at the bottom right of the sub-figures indicate the elapsed time. The scale bar at the bottom right is 1 cm.

To understand the role of the boundary on the onset of cracks, we first coated the vertical rim of the Petri dish with vacuum grease to minimise sample-boundary adhesion. The data, plotted in Supplementary Information Fig. S9(a), reveals the complete absence of elongative strains and very slow development of differential strains in the sample. The sample detaches from the vertical boundary and eventually shrinks laterally, giving rise to compressive strains throughout the sample. In this case, formation of the first crack is significantly delayed when compared to the sample in the uncoated Petri dish (maximal sample-boundary adhesion condition).

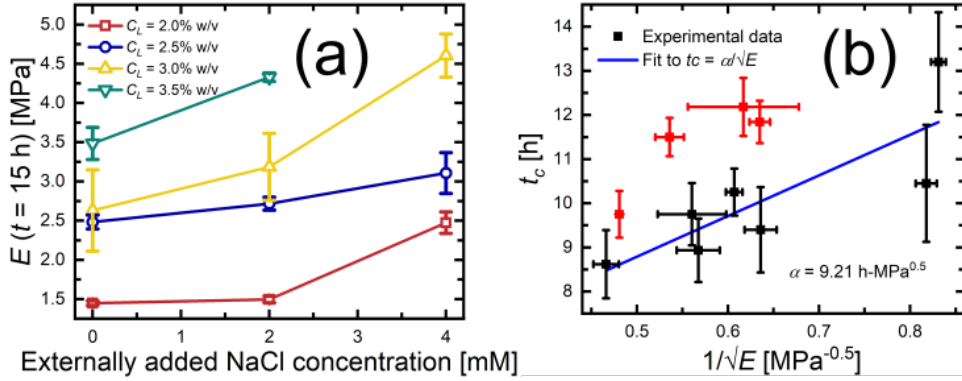
Next, we coated the vertical rims and bottom surface of the Petri dish with vacuum grease and tracked the temporal evolution of the strain field, shown in Supplementary Information Fig. S9(b).

Interestingly, in this scenario, the drying suspension shrinks but does not crack due to the uniform distribution of high compressive strains across the surface of the drying sample. Adhesion between the sample and boundary is therefore an important parameter for controlling the cracking and shrinkage of drying suspensions.

### ST3 Crack onset times and elasticity values

S. No.	Laponite clay concentration [% w/v]	NaCl concentration [mM]	Crack onset time $t_c$ [h]	Elasticity at $t = 14$ h [MPa]	Evaporation rate $V_E$ [m/s]
1	2.0	0	$13.20 \pm 1.13$	$0.99 \pm 0.11$	$9.75 \times 10^{-8}$
2	2.0	2	$10.45 \pm 1.33$	$1.41 \pm 0.05$	$9.75 \times 10^{-8}$
3	2.0	4	$9.40 \pm 0.97$	$1.63 \pm 0.23$	$9.75 \times 10^{-8}$
4	2.5	0	$11.84 \pm 0.48$	$1.24 \pm 0.06$	$9.75 \times 10^{-8}$
5	2.5	2	$10.25 \pm 0.53$	$1.78 \pm 0.18$	$9.75 \times 10^{-8}$
6	2.5	4	$8.93 \pm 0.72$	$2.83 \pm 0.27$	$9.75 \times 10^{-8}$
7	3.0	0	$12.18 \pm 0.66$	$1.92 \pm 0.06$	$9.75 \times 10^{-8}$
8	3.0	2	$9.75 \pm 0.71$	$2.33 \pm 0.10$	$9.75 \times 10^{-8}$
9	3.0	4	$8.62 \pm 0.77$	$2.93 \pm 0.25$	$9.75 \times 10^{-8}$
10	3.5	0	$11.50 \pm 0.43$	$3.76 \pm 0.31$	$9.75 \times 10^{-8}$
11	3.5	2	$9.75 \pm 0.52$	$3.69 \pm 0.16$	$9.75 \times 10^{-8}$

Supplementary Table S10: Tabulated values of crack onset time,  $t_c$ , estimated *via* direct imaging, and elasticity,  $E$ , of the fully developed clay gel at  $t = 14$  h, estimated in microindentation measurements, for different clay and salt concentrations and at different evaporation rates,  $V_E$ . The clay samples with the highest clay and lowest NaCl concentrations, marked in red, are expected to transform into nematic gels during the desiccation process.



Supplementary Fig. S11: (a) Elasticity values of partially dried clay suspension layers at elapsed time  $t = 15$  h, measured in microindentation experiments, are plotted *vs.* NaCl concentration for different clay particle concentrations. The standard errors are calculated from 4 measurements. (b) Crack onset time,  $t_c$ , *vs.* inverse square-root of sample elasticity,  $E$ . The blue line is a linear fit to the data ( $t_c = \alpha/\sqrt{E}$ ). Clay samples with the highest clay and lowest NaCl concentrations are depicted in red and are expected to transform into nematic gels during the desiccation process. The fracture energy, estimated from the slope  $\alpha$  of the fit, is approximately  $10^3 \text{ J/m}^2$ .

## ST4 Estimation of sample permeability using Carman-Kozeny relation

Sphericity  $\Phi_s$  measures how closely the shape of a particle resembles a perfect sphere. The sphericity of a clay particle of radius  $r = 12.5 \text{ nm}$  and height  $h = 1 \text{ nm}$  is calculated using [5]:

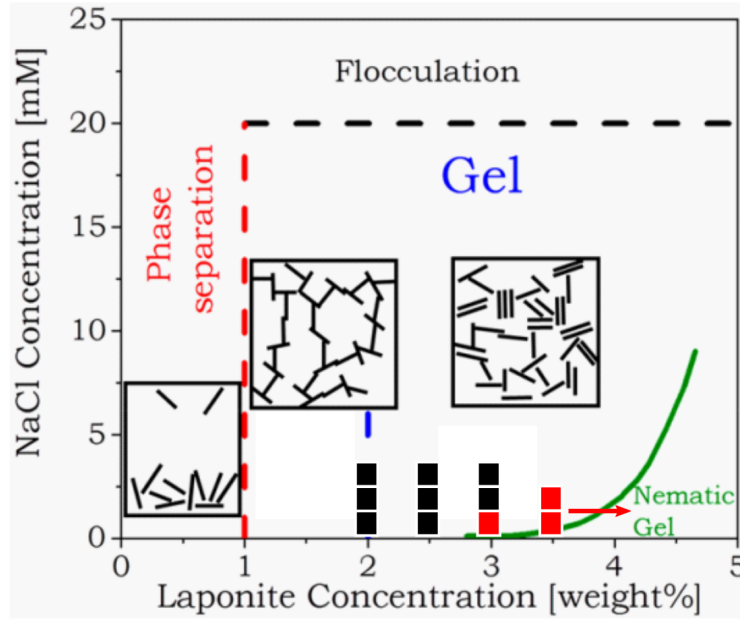
$$\Phi_s = \frac{\pi^{1/3}(6V_p)^{2/3}}{A_p}$$

Since the clay particle volume  $V_p = \pi r^2 h = 490.87 \text{ nm}^3$  and surface area  $A_p = 2\pi r^2 + 2\pi r h = 1060.30 \text{ nm}^2$ , sphericity  $\Phi_s = 0.28$  for a Laponite clay particle.

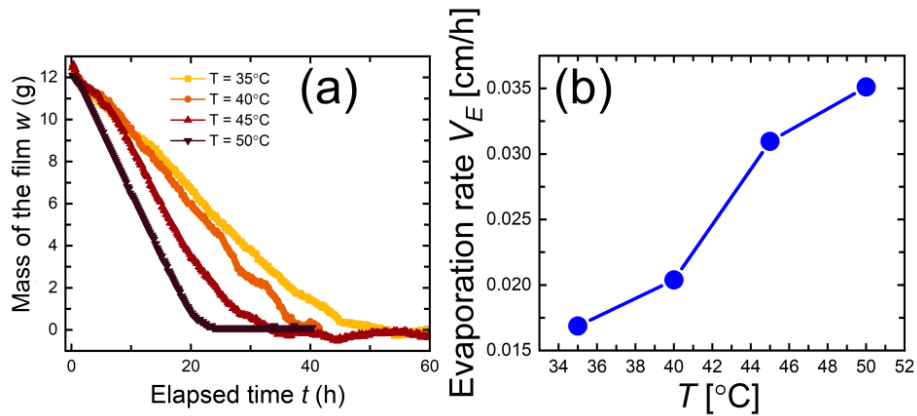
The permeability of the gel is determined using Carman-Kozeny relation [6] -

$$\kappa = \Phi_s^2 \frac{\epsilon^3 d_p^2}{180(1 - \epsilon)^2}$$

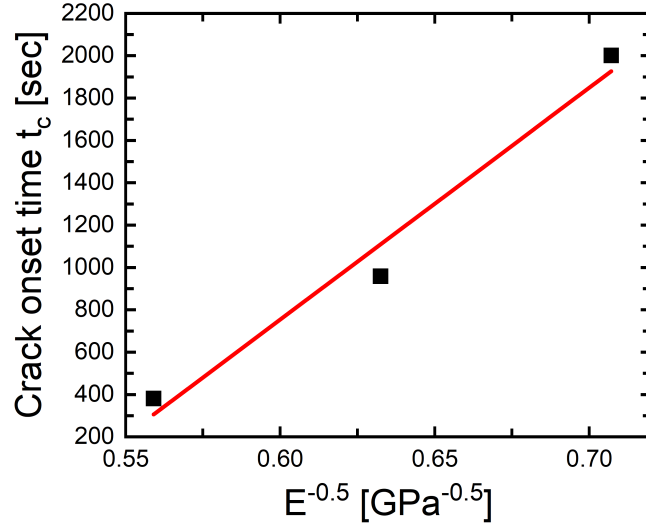
Using  $\epsilon = 0.8$  [7] as the porosity of the gel,  $d_p = 6.17 \text{ nm}$  as the diameter of the volume equivalent spherical particle, the permeability  $\kappa$  of the clay samples  $\kappa \approx 2.19 \times 10^{-19} \text{ m}^2$ .



Supplementary Fig. S12: Phase diagram of aqueous suspensions of Laponite clay as a function of clay particle and salt concentrations, reproduced with permission from [8]. All the drying samples used in our work were initially in the isotropic gel phase. The red points at the isotropic gel-nematic gel boundary are expected to transform into nematic gels over the course of the drying experiment and therefore deviate from the prediction of our model. These samples are marked in red in Fig. 5(b).



Supplementary Fig. S13: (a) Changes in sample masses with time due to desiccation at different chamber temperatures. (b) Evaporation rates,  $V_E$ , obtained from the slopes of the curves in the constant evaporation rate zone in (a), increase with increasing chamber temperature.



Supplementary Fig. S14: Crack onset time,  $t_c$ , for drying sessile droplets of concentrated silica gel [9], *vs.* the inverse square root of the silica gel elasticity,  $1/\sqrt{E}$  at  $t = t_c$ . The crack onset time data was extracted from [9] using the GRABIT program [10] in MATLAB, while the elasticity values were reproduced from Table 1 in [9]. The red line is a linear fit of this data to the prediction of our model,  $t_c \propto 1/\sqrt{E}$  (Eqn. 4 in the main manuscript).

## References

- [1] D. Arthur, S. Vassilvitskii, k-means++: the advantages of careful seeding, in: Proceedings of the Eighteenth Annual ACM-SIAM Symposium on Discrete Algorithms, SODA '07, Society for Industrial and Applied Mathematics, USA, 2007, p. 1027–1035.
- [2] N. Gavara, Combined strategies for optimal detection of the contact point in AFM force-indentation curves obtained on thin samples and adherent cells, *Sci. Rep.* 6 (1) (2016) 21267. doi:10.1038/srep21267.
- [3] W. F. Heinz, J. H. Hoh, Spatially resolved force spectroscopy of biological surfaces using the atomic force microscope, *Trends Biotechnol.* 17 (4) (1999) 143–150. doi:10.1016/S0167-7799(99)01304-9.
- [4] F. Carrillo, S. Gupta, M. Balooch, S. J. Marshall, G. W. Marshall, L. Pruitt, C. M. Puttlitz, Nanoindentation of polydimethylsiloxane elastomers: Effect of crosslinking, work of adhesion, and

- fluid environment on elastic modulus, *J. Mater. Res.* 20 (10) (2005) 2820–2830. doi:10.1557/JMR.2005.0354.
- [5] D. Wang, L.-S. Fan, Particle characterization and behavior relevant to fluidized bed combustion and gasification systems, in: F. Scala (Ed.), *Fluidized Bed Technologies for Near-Zero Emission Combustion and Gasification*, Woodhead Publishing Series in Energy, Woodhead Publishing, 2013, pp. 42–76. doi:<https://doi.org/10.1533/9780857098801.1.42>.
- [6] B. Kruczek, *Carman–Kozeny Equation*, Springer Berlin Heidelberg, Berlin, Heidelberg, 2015, pp. 1–3. doi:{10.1007/978-3-642-40872-4\\_1995-1}.
- [7] S. Ali, R. Bandyopadhyay, Effect of electrolytes on the microstructure and yielding of aqueous dispersions of colloidal clay, *Soft Matter* 12 (2016) 414–421. doi:10.1039/C5SM01700A.
- [8] K. Suman, Y. M. Joshi, Microstructure and Soft Glassy Dynamics of an Aqueous Laponite Dispersion, *Langmuir* 34 (44) (2018) 13079–13103. doi:10.1021/acs.langmuir.8b01830.
- [9] F. Giorgiutti-Dauphiné, L. Pauchard, Elapsed time for crack formation during drying, *Eur. Phys. J. E* 37 (5) (2014) 39. doi:10.1140/epje/i2014-14039-8.
- [10] J. Doke, GRABIT, <https://www.mathworks.com/matlabcentral/fileexchange/7173-grabit>, [Online; accessed March 22, 2024] (2024).